Thermal Properties of Nano- and Microstructures

Thesis by

Warren Chung Wah FON

In partial fulfillment of requirements for

the degree of

Doctor of Philosophy

California Institute of Technology

Pasadena, California

2004

Defended May 24th 2004

Acknowledgement

It is a pretty long journey before I am here to say thank you to many of whom that have made my graduate life so fruitful. First, I would like to thank Prof M L Roukes for granting me the opportunity and introducing me to the amazing world of NEMS. Thanks to Prof K Schwab for introducing me to the low T physics world, among other things, by showing me how a lock-in works and how to leak check. Thanks to Prof J Worlock for his butt-kicking suggestions to the work. Thanks to Nils Asplund and Steve Stryker and their wonderful pieces from the machine shop. Thanks to Dr Frank Monzon, Dr Darrell Harrington, Dr Mike Lilly, Dr Peter Burke, Dr Hong Tang, Dr Henry Huang and Dr Darron Young, Dr Henk Postma, Dr Dirk Orgassa, Prof Jim Hone, Dr Jan Honolka and Dr Carlo Callegeri. Also thanks to the fellows who are stuck here: Jack Yang (coffee time!), Wonhee Lee, Phillips Feng, Jessica Arlett, Ben Gudlewski and the long list of Roukes group member.

Finally, I really would to like to thank my parents, my grandma and my brother Otto for their support to me. My cousin William, his wife Denise and their son Blair who generously support a poor graduate student by feeding him. Last but not least is Tanya Lee the very cute, good girl.

Warren

Pasadena, California 2004

Abstract

My work is on the experimental study of thermal conduction in nano and microscale structures. The work is divided into two parts. In the first part, we measure the thermal conductance of a suspended device from 4 to 40 K. The thermal conduction of a suspended, free-standing beam is analyzed to study the effect of phonon scattering on thermal conduction. We conclude that phonon scattering is much more severe in a nanoscale beam than bulk material.

In the second part of the work, we proceed to dynamic measurement to measure the heat capacity of a suspended device. From that we study the origin of heat capacity of a silicon nitride membrane. We conclude that much of the heat capacity comes from the motional tunneling states of the ions. We use the device to demonstrate an ultrasensitive calorimeter with a very high resolution of 0.5 aJ/K. We conclude the work by applying the calorimeter to study the heat capacity of a thin adsorbed film of helium gas.

1 Thermal Properties of Nanostructures

1.1 The Mechanical aspect of Nanotechnology

In the past 10 years, we have seen the rise of nanotechnology as a major breakthrough in science and technology. It is a rare occasion when almost every branch of science and engineering can find interesting research under the same topic. Solid state physicists find a *new* dimension in the 1-D transport of nanotubes and nanowires.[1] Electrical engineers are utilizing these small components to build electrical circuit in order to keep the Moore's law rolling. Chemists are busy discovering new methods to prepare nanomaterials, making novel sensors and hoping to take over the electronic industry by self-assembling molecular electronics.[2] In the meantime, biologists simply realize that many biological systems, such as DNA or cell, are themselves delicate natural nanomachines.[3]

A very interesting, but yet not well explored aspect of nanotechnology is the mechanical properties of nanostructures. A nano-electro-mechanical-system (NEMS) is different from its bulk counterpart, as illustrated by the pioneering demonstration of mechanical oscillation exceeding 1 GHz at Caltech.[4] Because of the small size, displacement and force involved in nanoscale mechanical motion, the operation of NEMS depends sensitively on its immediate environment. In addition to traditional mechanical parameters such as Young's modulus and elasticity, mechanical motion of NEMS is affected by surface quality, surface adsorbants, chemical environment, etc.

On the downside, this complicated scenario leads to the mysterious quality factor reduction problem when shrinking NEMS. The good side, on the other hand, is the opening of NEMS as very sensitive and miniaturized sensors for mass detection and other nanomaterials, such as DNA.

Thermal conduction is another vital mechanical property of nanoscale structures with immense scientific and technological significance. Heat generation, conduction and dissipation in transistors are major challenges in the electronics industry. At cryogenic temperature, heat conduction engineering of micro-bolometers is a basic constituent for sensitive detection of radiation and energetic particles. In the research of themo-electric materials, improvement in the *figure of merit* (i.e. the ability of a material to carry electrical current but not heat current) is achieved in quantum dot superlattice and bismuth nanowires.[5] In scientific research, the heat conduction through a mechanical point contact measures the universal quantum of thermal conductance. Moreover, the electron-phonon interaction has been shown to behave differently in clusters and quantum dots.

1.2 Study of thermal properties of nanostructure at Caltech

The Caltech group led by Professor Roukes are pioneers in the measurement of thermal properties using suspended semiconductor nanostructures with sensitive *in-situ* thermometry and application in ultra sensitive bolometry and calorimetry. The use of suspended structures greatly increases the experimental difficulties but provides a clear, well-defined path for heat to flow. It also improves thermal insulation which is a key for construction of sensitive bolometers and calorimeters. Early work by Dr. Tom Tighe and Dr. Keith Schwab include first thermal conductance measurement of suspended nanostructure with in-situ, separate heaters and thermometers and the measurement of the universal quantum thermal conductance.[6,7]

My work, which is detailed in the following sections, is mainly divided in two parts. First, I extended the measurement of thermal conductance of nanostructure similar to that studied by Tighe and Schwab to higher temperatures (4 to 40 K).[8] In this temperature range, the thermal conduction becomes heavily influenced by the scattering of phonons. Thus, the measurement provides a key understanding to phonon scattering in nanostructures. Second, I implemented a dynamic measurement on the nanostructure to capture its thermal relaxation in order to deduce the heat capacity. This makes it possible to determine the density of states (DOS) of phonon and other tunneling motion and open the path for the observation of dimensional crossover of phonon DOS. Finally, I employ the nanostructures to realize an ultra sensitive calorimeter and measure the heat capacity of an adsorbed film of Helium 4 gas.[9]

2 Phonon Thermal Transport in Nanostructures

2.1 Introduction

In this study, we report the measurement of thermal conductance of n-doped and intrinsic (undoped) mesoscopic GaAs beams from 4 to 40 K. This follows the earlier measurement of similar structures at lower temperature performed by Tighe *et al* and Schwab *et al*. At intermediate temperatures, phonon thermal transport is strongly influenced by the scattering of phonons. While phonon transport and scattering mechanisms in bulk crystalline GaAs and other semiconductors are well known,[10,11] no systematic study has been carried upon nano-scale semiconductor structures. Early works on suspended submicron-diameter beams found that thermal transport due to electron dominates over phonon.[12] This is because the weak electron-phonon coupling at low temperature limits the amount heat transferred into the lattice.[13] Later work by Tighe et al. on suspended structure with separate heater and thermometer reduced undesired conduction through the diffusion of electron and found that phonons are the major carriers of heat energy above 2 K. They also conclude that the dominant scattering mechanism below 10 K is diffusive phonon surface scattering.

Here, we describe a measurement in which additional scattering mechanisms, such as electron scattering, impurity scattering and Umklapp phonon-phonon scattering, are studied. Electron-phonon and impurity phonon scattering are investigated by comparing the thermal conductance of an intrinsic (undoped) GaAs beam and a $n+$ bi-layer GaAs beam with similar geometry. Umklapp scattering is studied by extending the measurement to higher temperature (>20 K) when the process is turned on in bulk sample.

In the following sections, we will first detail the experimental procedures, including the fabrication of device, the operation of cryogenics and the measurement technique including noise reduction. Then, after presenting the thermal conductance data, we will analyze them following the Callaway's analysis,[10] a traditional mean for establishing the relation between thermal conduction and phonon scattering in bulk material. Finally, we will discuss the scattering of phonons by characterizing the respective scattering rates and comparing them with their analogs in bulk systems.

2.2 The thermal transport nanodevices

The devices are fabricated from GaAs heterostructures grown by molecular beam epitaxy. The topmost layer is 500 Å of degenerately Si doped, *n*+ GaAs ($N_D = 2 \times 10^{18}$ cm^{-3}). It is patterned into two meandering strips to form electrical transducers acting as heat source and temperature sensor. The second layer is 1000 Å thick undoped *i*-GaAs that forms the isolated reservoir and thermal conducting beams. The third $Al_{1-x}Ga_xAs$ sacrificial layer ($x \approx 0.2$) is removed during the fabrication to suspend the structure with a ≈1 μm gap from the GaAs substrate.

The experiment involves measurement on two sets of suspended devices. They contain two kinds of beams for thermal conduction. The first set of devices, called the *4-beam* *devices*, is shown in Fig. 1. It consists of four 6 μm long, 250 nm wide and 1500 Å thick *bi-layer beams*. Fig. 2 shows the cross section of the bi-layer beam and note only the top one third of the beam is n+ doped while the rest is undoped. The second set of devices, called the *6-beam devices* (Fig. 3), contains two more *undoped beams* in additional to the four bi-layer beams. All the bi-layer beams on both devices have the same dimensions. But the undoped beam is only 1000 Å thick (Fig. 4).

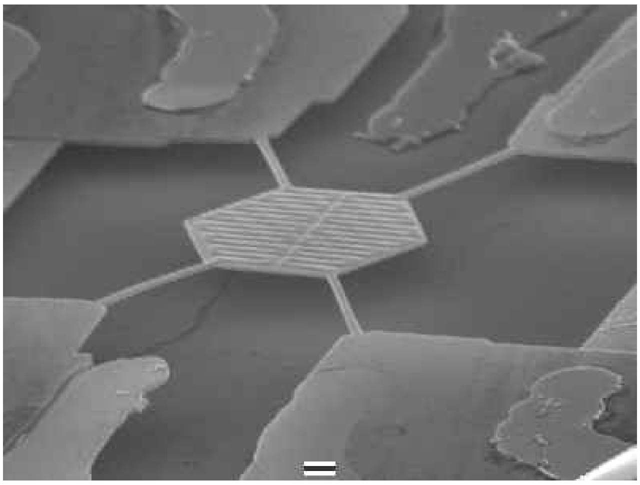

Fig. 1 The 4 beam device. The device has 4 bi-layer beams as described in Fig. 2.

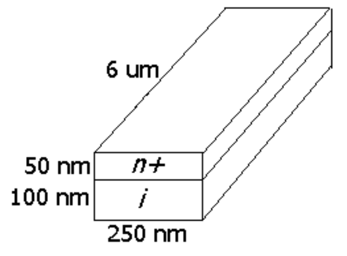

Fig. 2 The dimension of a bi-layer beam

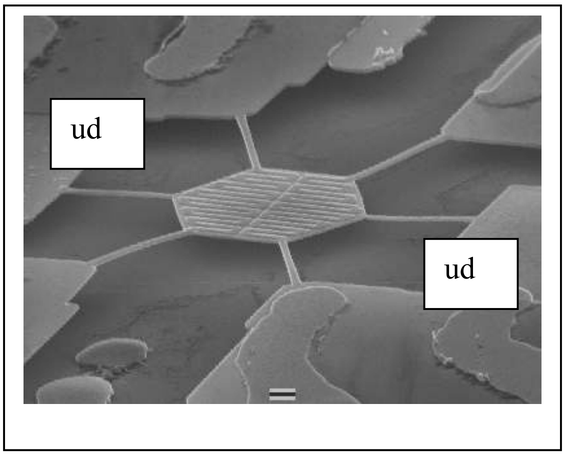

Fig. 3 The 6 beam device. It has 4 bi-layer beams and 2 undoped beams as described in Fig. 2 and Fig. 4. The undoped beams are those marked “ud” in the fig.

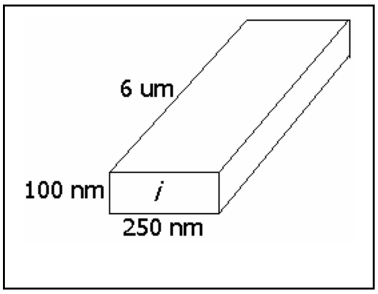

Fig. 4 An undoped beam

2.2.1 The *n*+ GaAs resistive heater and resistance thermometer

The two meanders formed from the *n*+ GaAs are electrical transducers acting as a heat source and a resistive temperature sensor. The temperature dependence of resistance of *n*+ GaAs at low temperatures comes mainly from the weak localization of electrons. The meander pattern ensures most of the resistance of the transducers lies on the cavity where heat is to be generated and temperature to be sensed. Some of the heat is dissipated on the beams. The *n*+ GaAs has major advantages over the usual metals (e.g., gold) as electrical transducers. First, it is part of the crystalline structure of the GaAs and thus minimizes the amorphous defects otherwise introduced by metal deposition. Second, a heavily doped semiconductors have a much lower carrier density ($\approx 10^{18}$ cm^{-3}) than the usual metals ($\approx 10^{23}$ cm^{-3}) and that greatly reduces thermal conduction by electrons, an effect to be minimized in the measurement of phonon thermal conductance. The major disadvantage of the low carrier density is the resultant high thermal resistance between the electron and phonon systems. As a result, the electron temperature in the heater can be strongly decoupled from the lattice. Therefore, a separate thermometer with very small heat dissipation is necessary for accurate measurement of phonon temperature (details in following sections).

2.2.2 The Detailed Procedure of Fabrication

The following is a detailed procedure of fabrication of the GaAs device.

a. Wafer cleaning

- Begin with a piece of GaAs wafer with the following composition (from top to bottom): 750 Å *n*+ GaAs ($N_D = 2 \times 10^{18}$ cm^{-3}), 1000 Å *i* GaAs ($N_D = 2 \times 10^{15}$ cm^{-3}), 1 μm AlGaAs (sacrificial layer), 720 Å *i* GaAs and substrate.
- Clean the chip and remove the protective photoresist (PR) in acetone on a hot plate of 100°C for 15 mins. Rinse in IPA. This is also the general cleaning procedure after liftoff.

b. Formation of ohmic contact

- Ohmic contact to *n*+ GaAs is necessary for external electrical connection to the device.
- Define bond pads by positive optical lithography. Spin PR AZ 5214E at 4000 rpm (revolutions per minute) for 60 s. Bake at 95 °C for 2 mins. Expose the bond pad pattern as mask aligner for 15 s at a UV light intensity of ≈ 15mW/cm^2. Develop in AZ developer for 15 to 30 s. Blow dry and clean in ozone stripper for 5 mins.
- Deposit 430 Å of Ge, 200 Å of Ni and 870 Å of Au by thermal evaporation. Liftoff in acetone. Clean chip.
- Anneal at 450 °C for 1 min at the annealing station.

c. Bond pads

- The Au bond pads are to promote adhesion for wirebonding and to protect the ohmic contacts.
- Define bond pads by optical lithography using a positive resist.

- Deposit 50 Å of Cr and 1500 Å of Au by thermal evaporation. Liftoff in acetone. Clean chip.

d. Finger pads

- The major purpose of the finger pads is for electrical contact, alignment and as etch mask
- Define bond pads by positive optical lithography.
- Deposit 500 Å of Ti, 50 Å of Cr and 500 Å of Au by thermal evaporation. Liftoff in acetone. Clean chip.

e. Alignment marks for electron beam (ebeam) lithography

- Spin PMMA bi-layers: first, spin PMMA 495K-C at 3500 rpm for 60 s. Bake at 180 °C for 5 mins. Repeat for the PMMA 950K-C.
- Load the chip into the SEM. After starting up SEM according to procedure, find a spot on the chip to adjust focus and astigmatism at 100,000 ×.
- Find another spot which is close (~100 μm) to the spot of ebeam writing and "burn" a spot on the PMMA by focusing the ebeam in the spot mode for 45 s. Check for a stigmatism and further adjust the focus.
- Move and zoom to the writing spot at 1000 ×. Coarse align on the screen using the transparency.
- Write the pattern by the Nano-pattern-geneartion-system (NPGS) program using the *run file* c4a.rf6. The Design CAD pattern file is cond07.dc2.

- Develop in MIBK:IPA = 1:3 solution for 1 min. Rinse in IPA and blow dry.
- Deposit 50 Å of Cr and 800Å of Au by thermal evaporation. Liftoff and clean chip. Inspect under optical microscope and SEM.

f. Patterning of meander transducers

- We fabricate the *n*+ GaAs meander by etching with a Ti mask.
- Define the meander pattern c4b.rf6 by ebeam lithography. After aligning at 1000 ×, beam current 10 pA and condenser lens of 14, write the first layer. When the NPGS pauses, turn the magnification to 800 ×, ebeam current to 90 pA at condenser lens of 11 and write the second layer.
- Develop the chips and deposit 850 Å of Ti in the ebeam evaporator. Liftoff.
- Etch in the Chemical Assisted Ion-beam E tch (CAIBE) with 0.2 mTorr of Ar and 0.4 mT of Cl at 20 mA beam current and 1500 V for 12 s.
- Check for completion of etch by probing for electrical isolation between pair of meanders.

g. Cavity

- The cavity is defined similar to the meanders
- Run NPGS run files c4c.rf6 for 4 beam device or c4d.rf6 for 6 beam device. For the first layer, write at 1000 ×, ebeam current of 10pA and condenser lens of 14. After the pause, change to 700 ×, ebeam current of 90 pA and condenser lens 11 and write the second layers.

- Deposit 850 Å of Ti by ebeam evaporator.
- Etch in the CAIBE for 90 s.
- The etch goes into the AlGaAs sacrificial layer. The Au finger pads are gone but the Ti below remains. The Ti deposited for the meander in the previous step acts as the mask for the beams.

h. Undercutting the sacrificial layer

- Prepare the following solutions according to the order of dipping: 52% HF: HNO_3: H_2O = 5: 2: 10, 100% ethanol, KOH: H_2O = 5 g: 100 g, three beakers of 100% ethanol. Stir the solutions well. Use a Telfon holder to hold the chip.
- Dip the chip in HF for 35 s.
- Dip the chip in ethanol for 30 s and the KOH solution for 1 min.
- Clean the chip in the 3 beakers of ethanol.
- Keep the chip wet in the ethanol. Secure it to the holder for critical point drying.
- The etch removes the AlGaAs sacrificial layer and the remaining Ti masking material.

i. Critical point drying

- Check the critical point dryer for leaks and test run it.
- Fill the dryer boat with 100% ethanol.
- Put the chip into the ethanol on the boat, load the boat into the chamber and seal it. Quickly fill the dryer with liquid carbon dioxide. Make sure

the temperature of the chamber is below 21 °C. The filling pressure is 800 psi.

- Wait for 5 mins for ethanol to settle to the bottom.
- While keeping the L CO_2 supply on, flush out the ethanol. Shake the chamber to get rid of ethanol trapped near the bottom of the front window.
- Stop the CO_2 supply. Seal all the valves. Turn on the heated water supply.
- The critical point of CO_2 is at 32 °C. At that point the liquid vapor interface disappears.
- When the dryer reaches 36 °C and 1200 psi, release the pressure slowly. It should take ≈ 15 mins to release the pressure.
- After reaching the atmospheric pressure, open the chamber and take the sample out.

j. Post fabrication check list

- The device should be clean. No Ti or fluffy cloud of dirt should remain
- The resistance of the meander is ≈ 60 kΩ.
- The resistance of the finger is ≈ 3 kΩ.
- Inspect under the SEM for suspension and complete undercut at tilted angle.

2.3 The Principle of Measurement

The total phonon thermal conductance of the beams of the nanostructure is defined as:

$$G_{Ph}(T) = \dot{Q} / \Delta T \qquad \text{Eq. 1}$$

where ΔT is the rise in phonon temperature in the cavity induced by the heating power $\dot{Q}$. The heating power, $\dot{Q}(2\ to\ 200\,nW)$, is the Joule heat dissipated in the heater due to a DC current. The heating power is limited so that the resultant rise in temperature is ≈5 % of the base temperature to insure linear response. The temperature rise is sensed as a resistance change in the resistance thermometer probed by 4-point-probe lock-in technique. The thermometer probe current is kept small (≈ 10 nA) to prevent electron heating so as to acquire a accurate measurement of the phonon temperature.

2.4 The Experimental Setup

2.4.1 The 1-K Dipper and Sample Mounting

The cryostat used is a home-made 1-K “dipper” which is immersed into liquid helium for low temperature measurements. The sample is mounted in a ultra high vacuum (UHV) environment and cooled to the low temperature by liquid helium. The temperature of the sample stage is further controlled by a Lakeshore NTD Ge thermometer, a resistor heater and a Lakeshore temperature controller to a resolution of ≈ 10mK. The thermalization time of the sample stage increases from 1 to 15 mins when temperature is raised from 4 to 40 K. The chip of the device is first glued and wire-bonded to a special holder which is then mounted to the dipper. Electrical connections from the bottom to the top of the dipper are made of manganese twisted pairs for low thermal conduction. The dipper is sealed, pumped and leak checked before the cool down.

2.4.2 The Electrical Measurement Setup

2.4.2.1 The Basic Technique and Resolution of Measurement

We first discuss here the basic, ideal concept of the measurement. First, the resistance of the resistive thermometer is monitored by 4 wire low frequency lock-in technique with a small sensing current I_{Th} = 10 nA. The frequency of the lock-in is limited below 100 Hz due to the large capacitance of the twisted pairs (~ 1 nF). At a thermometer resistance of 60 kΩ, the roll off occurs at ≈ 2 kHz. The resistance of the thermometer is recorded when the temperature of the sample stage and device is ramped from 4 to 40 K by the dipper's temperature control to calibrate the $n+$ GaAs resistitive thermometer. Next, a DC current, I_H = 0.2 – 2 μA, is passed through the heater to heat up the device. The resistance change of the thermometer is recorded to determine the temperature rise of the device through the calibration.

The accuracy of the measurement is mainly limited by the resolution of the thermometry. The pre-amplifier used to monitor the thermometer has a typical noise of 5 nV/√Hz. According to the manual of the Stanford lock in, the noise equivalent bandwidth (NEBW) of the lock-in is $5/64\tau$. At a time constant of $\tau = 3$ s, the input noise is thus $v_n = 5\,nV/\sqrt{Hz} \times (5/64/3\,Hz)^{1/2} = 0.8\,nV$. The sensitivity of the resistance thermometer is $\partial R/\partial T \approx -200\ \Omega/K$. Thus, the resolution of the thermometry is $\Delta T_n = v_n / I_{Th} / |\partial R/\partial T| = 0.4\,mK$. Since the rise of temperature due to heating is 5 % of substrate temperature, the lowest resolution of thermometer signal is 0.5 % at 4 K, which is an appropriate resolution for our measurement.

However, reality is always less than ideal. Below, we will discuss the two major problems degrading the resolution and the respective solutions. These include ground loop noise and the digitization limit of the lock-in.

2.4.2.2 Elimination of Ground Loop noise by Optical Isolators

Ground loop noise refers to the imperfection of ground among different parts of the circuit. As a result, the ground at the device is fluctuating with respect to the ground of the amplifier at low frequency, thus generating noise. The major problem of ground loop noise is that it can fall in the very low frequency (< 1 Hz) and thus could not be reduced by averaging. In fact, long averages (> 1 s) tend to deteriorate the signal. In our setup, the ground loop noise could produce fluctuations as large as 30 Ω at a time scale of 1 hour and practically kill the measurement.

Apart from connecting different grounds of the circuit and equipment by heavy wire strips, a very reliable way to eliminate ground loop noise is to “break the ground” by equipment such as optical isolators like Burr Brown ISO 120. With such a setup, we improve the stability of resistance measurement to below 2 Ω for over a period of 24 hours. The major disadvantage of an optical isolator is its high intrinsic input noise of ≈ 4 μV/√Hz. Thus, signal is to be maximized before going through the optical isolators.

2.4.2.3 Elimination of Digitization Noise by Bridge Circuit

The resolution of a lock-in measurement is not limited only by the input noise. Consider measuring the 60 kΩ thermometer by a 10 nA probe current. The lock-in range is set to 1 mV to measure the voltage of 600 μV. For a 12-bit digital analog converter at the input of the lock-in, the minimum resolvable voltage is 240 nV, or equivalently 24 Ω. This forbids us from achieving the desired resolution despite the low noise. One may wonder if the problem is irrelevant if an analog lock-in is used. However, it is also a very difficult task to read the output of an analog lock-in, which is simply a DC voltage, accurately down to 1 part in 50,000 to achieve the desired resolution.

A solution to the problem is by the use of a bridge circuit. An impedance box is added in series to the resistance thermometer in order to reduce the signal fed into the input of the lock-in. A simple way to construct an impedance box is a combined voltage divider and phase shifter. With such setup and careful manual tuning of the impedance box, over 99.5 % of the signal is offset. The digitization noise is effectively reduced by 99.5 % to 0.2 Ω and is no longer significant.

2.4.2.4 A detailed schematic of the measurement

A detailed schematic is shown in Fig. 5. A HP DC power supply is used to current bias the heater. The thermometer signal is amplified by an EG&G 5006 voltage amplifier before being measured by a Stanford Research SR830 lock-in amplifier. The Burr Brown ISO120 optical isolators separate the grounds between the device and AC powered electronics. The device ground is isolated and is powered by ±18 V rechargeable lead-acid batteries. To prevent the noise of the optical isolators from degrading the signal, the heater power supply passes a large voltage through the isolator before attenuated to the desired level. On the thermometer side, the signal is amplified by the pre-amplifier before being fed into isolators.

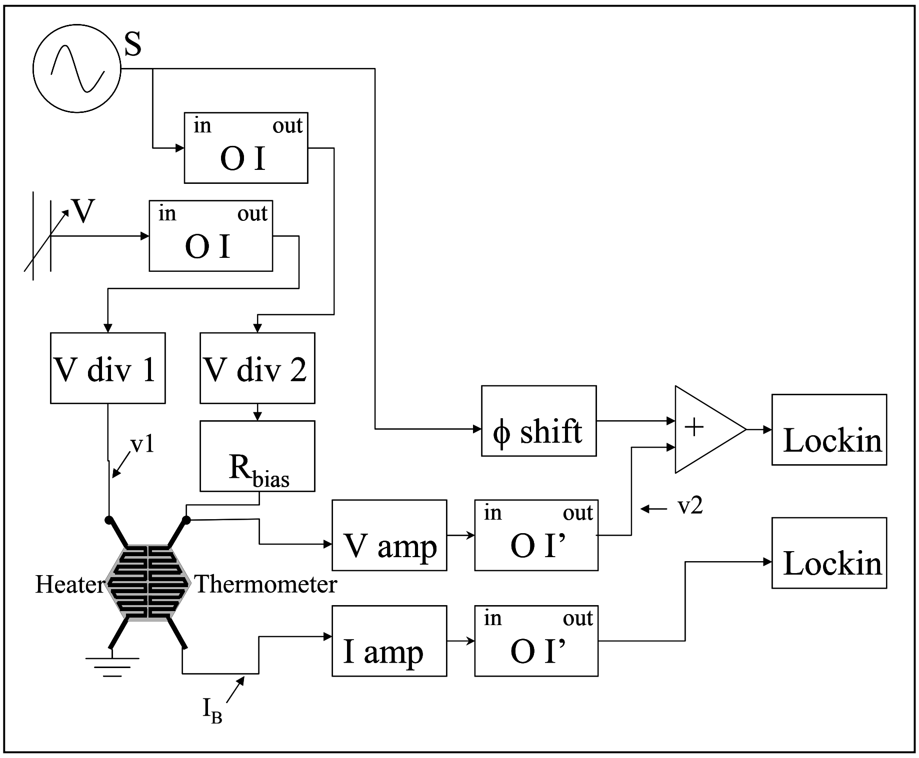

Fig. 5 A detailed schematic of thermal conductance measurement. S is the sine source, OI are the input optical isolators and OI' are the output optical isolators. V div is voltage divider. V amp and I amp are voltage and current amplifier respectively. ϕ shift is the phase shifter.

2.5 Experimental result

2.5.1 The Calibration of GaAs Thermometer

After the device is cooled down to cryogenic temperature in high vacuum, the first step of the measurement is the characterization of the *n*+ GaAs resistance thermometer. We calibrate the GaAs thermometer at 10 nA against a commercial NTD Ge thermometer. The calibration shown in Fig. 6 is slightly sample dependent. But it is highly reproducible over time and after repeated cool-downs for any given device. The temperature sensitivity of the thermometer, $\partial R/\partial T$, is plotted in Fig. 7. It is approximately -130 Ω/K at 4 K and reduces to -20 Ω/K at high temperature.

During the calibration, the temperature of the sample stage is controlled by the heater and Ge thermometer and has a thermalization time of 5 to 15 mins. The temperature of the GaAs thermometer, however, takes another 5 to 10 mins to approach the steady state. This is because the device is primarily cooled by the bonding wires and thus has a long thermalization time.

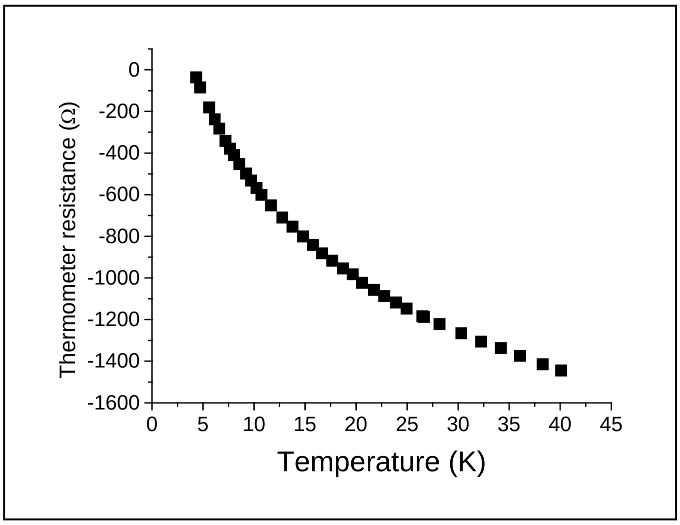

Fig. 6 The temperature dependent resistance of the GaAs thermometer. Because bridge circuit is used for measurement, the absolute resistance of the thermometer is not shown.

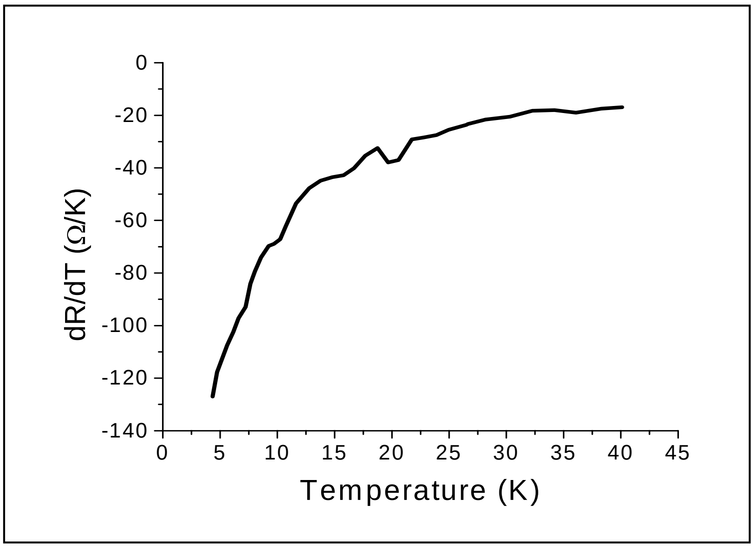

Fig. 7 The temperature sensitivity of the GaAs thermometer

2.5.2 Resolution and Stability of the GaAs thermometer

The experimental resolution and stability of the resistance of the GaAs thermometer is demonstrated in Fig. 8 for a bias current of 10 nA at 4 K. The lock-in is set at the frequency of 17 Hz and a time constant of 1 s. The rms resolution of the resistance measurement is 2 Ω. The resistance value is stable up to 24 hrs. Note that due to the slow thermalization of the sample stage, a complete measurement from 4 to 40 K takes up to 12 hrs.

2.5.3 Electron-phonon coupling in the thermometer

Electron-phonon coupling is a key to this experiment for both the heater and the thermometer. In

Fig. **9,** we plot the resistance of the thermometer versus the bias current at 4 K. The resistance drops upon application of a high bias current due to the hot electron effect. Namely the temperature of the electrons stay higher than that of the phonons. To obtain accurate measurement of the phonon temperature, the thermometer bias current has to be kept at the low value regime. We use 10 nA thermometer bias current exclusively in the calibration and conductance measurement. It is a current value known to provide insignificant electron-phonon decoupling.

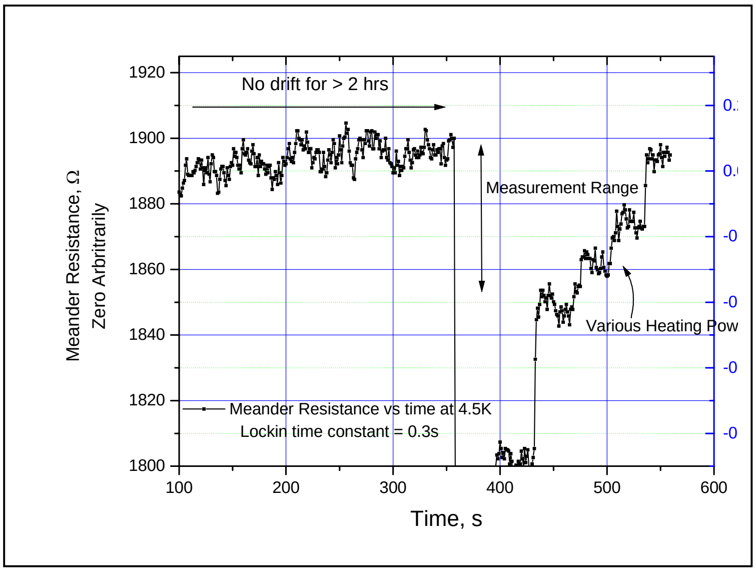

Fig. 8 The resistance of GaAs thermometer: Before t = 350s, the thermometer shows small drift for over 2 hrs to demonstrate its stability. Afterward, heat is applied to the heater to change the resistance of the thermometer.

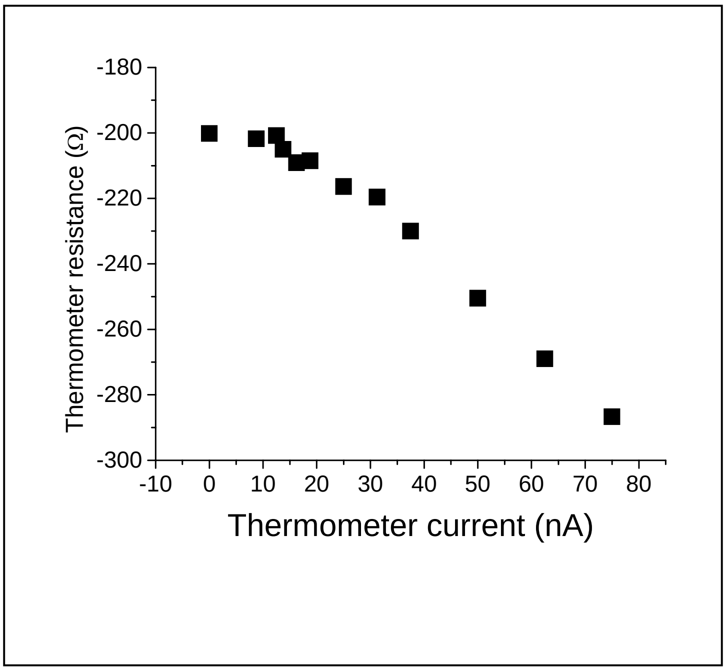

Fig. 9 The change in resistance of the thermometer versus probe current. The absolute value of the resistance is not shown

2.5.4 Heat dissipation in the heater

To ensure an accurate measurement, the Joule heating generated in the heater ideally must be completely transferred into the lattice. Nevertheless, as mentioned in the last section, electron-phonon coupling is weak at cryogenic temperatures. As a result, energy in the heater could alternatively be carried out through the electrical transducer by electron diffusion. We could not distinguish the contribution of the two pathways in our experiment. The dissipation of heat from the electrons in the heater (to phonon and by diffusion) is plotted in Fig. 10. We will discuss this dissipation in detail in section 2.7.2.

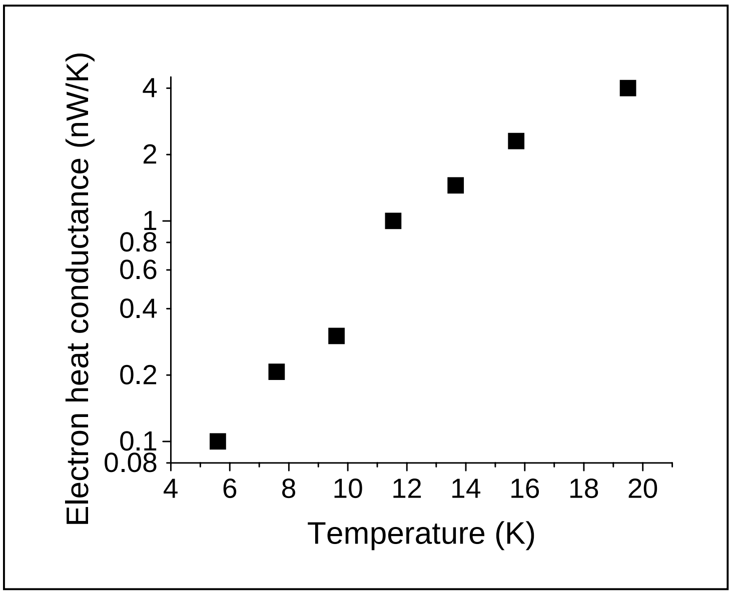

Fig. 10 The electron thermal conductance in the heater

2.5.5 Measurement of phonon thermal conductance

I will detail in this section the measurement of the thermal conductance. The data over the range of temperatures are found in the next section. After the thermometer is calibrated, the sample stage is set to the desired base temperature (4 K in the following example). Then, the resistance of the GaAs thermometer is monitored until it stabilizes. This indicates that the sample is thermalized to the base temperature. Next, a DC heating power is applied onto the device through the heater. In the mean time, the drop in the thermometer resistance, ΔR_t, is recorded. From the calibration chart, the respective change in device's temperature, ΔT, is determined. The power, $\dot{Q}$, is obtained by applying a known voltage, V_h, to the heater resistor R_h. Finally, the phonon thermal conductance, G_{Ph}, is obtained as:

$$G_{Ph}(T) = \dot{Q}/\Delta T = (\frac{V_h^2}{R_h})/(\frac{\partial T}{\partial R_t}\Delta R_t) \qquad \text{Eq. 2}$$

We plot in Fig. 11 $\dot{Q}$ versus ΔT at 4 K. At low heating power, the points follow a linear relation. When $\dot{Q}$ exceeds 4 nW, ΔT deviates from the linear response and becomes smaller than expected. This is because the strong heating significantly elevates the temperature of the device and increases the phonon thermal conductance. To obtain an accurate measurement of the conductance at temperature T, therefore, $\dot{Q}$ has to be small enough so that ΔT does not exceed ≈ 5 % of T. From Fig. 11, we obtain the thermal conductance as the inverse of the slope in the part of linear response regime.

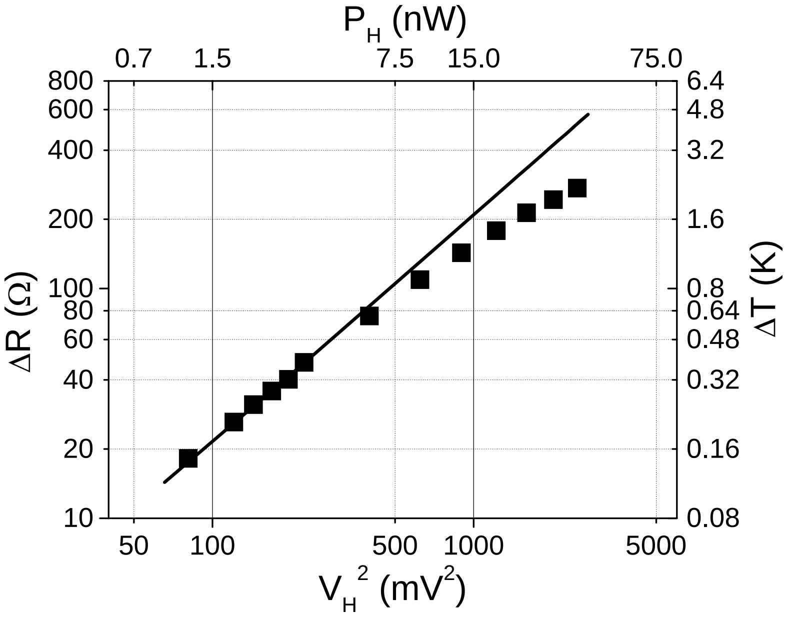

Fig. 11 The temperature change in the device versus applied power at 4.7 K

2.5.6 Phonon thermal conductance

We performed measurement of thermal conductance on four pairs of 4 and 6 beam devices from 4 to 40K. Except for one pair showing significantly higher conductance (we believe that happened because the sacrificial layer below these particular devices were not completely removed), the rest show similar results. In Fig. 12, we plot the measured thermal conductance from a pair of devices. There is a significant difference between the conductance of the the 4 beam and 6 beam devices, indicating that the extra leads are very effective in conducting heat. In the following sections, we will analyze the data and extract information regarding phonon scattering.

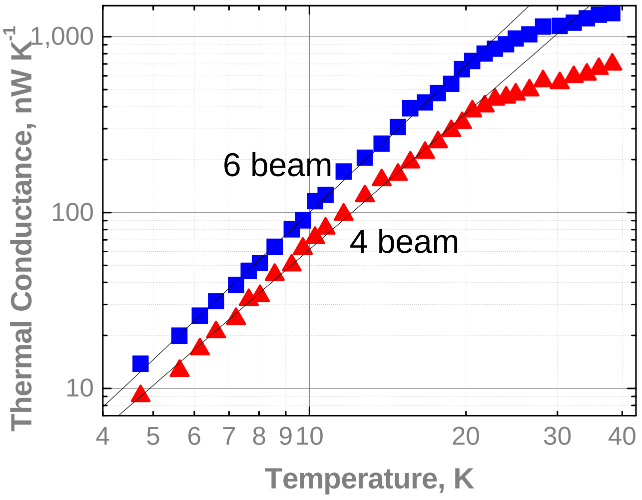

Fig. 12 The thermal conductance of the 4 beam and 6 beam devices

2.6 Data Analysis of thermal conductance measurement

2.6.1 The phonon thermal *conductivity*

In our analysis, we focus on the thermal conductance of an *individual* suspended beam. For a four-beam device, *one quarter* of the total thermal conductance represents the thermal conductance of a single bi-layer beam. To deduce the phonon thermal conductance of a single *undoped beam,* we subtract from the total conductance of the six-beam device the contributions from the four bi-layer beams, as deduced from the four-beam device, and divide this by 2. Stated equivalently, the conductance of a single undoped beam is deduced as *one-half of the difference* between the total conductance of the 6 and 4-beam devices. This subtractive comparison is valid if the two devices are identical except for the two undoped beams. Final inspection of our devices by scanning electron microscopy confirms that difference in dimension are less than 5%.

Next, in order to compare the thermal conduction in leads of different dimension and conduction in bulk material, we define the so-called *effective thermal conductivity* $g = G\, l / A$, where l is the length and A is the cross section area of a beam. We plot the effective conductivity of a bi-layer and an undoped beam in Fig. 13. Note that the conductivity of the undoped beam is significantly higher than that of the doped beam.

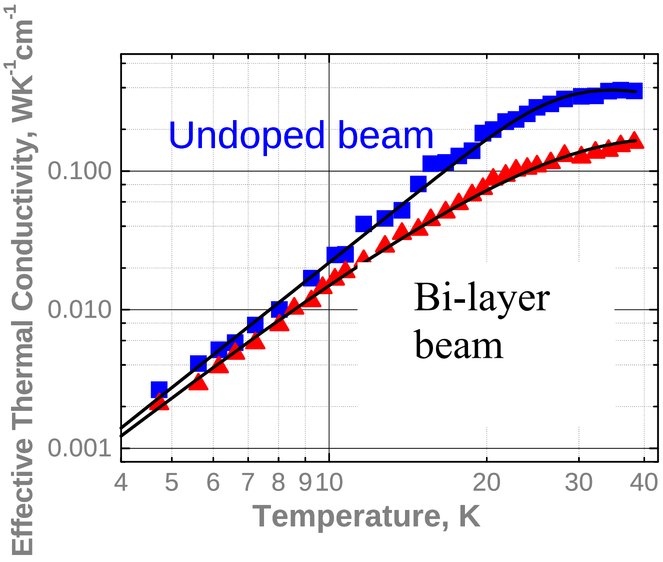

Fig. 13 The effective thermal conductivities of the bi-layer and undoped beams

While the notion of effective conductivity is helpful for comparison and extraction of scattering rates (discussed later), it must be exercised carefully in the microscopic regime when ballistic transport could be dominant. This is because in the ballistic regime the conductance is no longer inversely proportional to the length of the beam. Hence, conductivity becomes an ill-defined quantity. An easy criteria to avoid this scenario is to compare the phonon mean free path $\lambda = 3Gl / CcA$, where C is the phonon heat capacity and c the velocity of sound to the length of the beam *l*. Only when $\lambda << l$ is the conductivity a well defined quantity. In our experiment, as discussed below, this is a valid statement, as $\lambda \approx 1$ μm and $l = 6$ μm.

2.6.2 A theoretical framework for scattering of phonons

2.6.2.1 The Boltzmann equation for transport of phonons

Before analyzing the data, we first provide a framework of theoretical analysis which links phonon thermal conduction to its scattering. The most basic equation of transport is the Boltzmann equation.[14] The phonon conduction of a beam is defined as:

$$\mathbf{G} = \sum_k \hbar\omega(\mathbf{k})\mathbf{c}(\mathbf{k}) f(\mathbf{k}) \qquad \text{Eq. 3}$$

Where the summation is over all possible values of k in the momentum space, ω is the angular frequency and c the group velocity of the phonon. The key undetermined factor in the equation is *f*(k), the occupation factor of the modes, which is governed by the Boltzmann equation as:

$$\frac{\partial f}{\partial t} = \frac{\partial f}{\partial t}_{Drift} + \frac{\partial f}{\partial t}_{Scattering} = 0 \qquad \text{Eq. 4}$$

The drift term accounts for change in occupation factor due to temperature gradient and the scattering term accounts for the change due to various scattering mechanisms. Their overall sum is zero because in a steady state, the occupation factor is constant with time. The drift term is linked to the spatial variation in temperature as:

$$\frac{\partial f}{\partial t}_{drift} = -(\mathbf{c} \bullet \nabla T)\frac{\partial f}{\partial T} \qquad \text{Eq. 5}$$

Given the complexity of scattering events, there is no complete solution for the scattering term. A commonly adopted solution is the so-called relaxation time method in which the occupation factor is restored to the thermal equilibrium one due to the scattering in a relaxation time τ:

$$\frac{\partial f}{\partial t}_{drift} = \frac{f^\circ - f}{\tau} \qquad \text{Eq. 6}$$

Generally, τ is assumed to depend only on the frequency of the mode and the temperature. We combine Eq. 4, Eq. 5 and Eq. 6 to find that in one dimension:

$$c^z \frac{\partial f^\circ}{\partial T}\frac{\partial T}{\partial z} = \frac{f^\circ - f}{\tau} \qquad \text{Eq. 7}$$

Where c^z is the speed of the phonon in the z direction (direction of the beam). We may then solve for G by noting that thermal conduction in thermal equilibrium vanishes:

$$G = \sum_k \hbar\omega(\mathbf{k})(c^z)^2 \tau \frac{\partial f^\circ}{\partial T}\frac{\partial T}{\partial z} \qquad \text{Eq. 8}$$

And the thermal conductivity:

$$g = \frac{G}{\partial T / \partial z} = \sum_k \hbar\omega(\mathbf{k})(c^z)^2 \tau \frac{\partial f^\circ}{\partial T} \qquad \text{Eq. 9}$$

$$= \frac{1}{3}\int_0^{\omega_{\max}} \hbar\omega c^2 \tau \, n(\omega) \frac{\partial f^\circ}{\partial T} d\omega$$

Where n is the density of state of phonons. By applying the Debye phonon model for the density of states, we conclude that:

$$g = \frac{k_B}{2\pi^2 c}(\frac{k_B}{\hbar})^3 T^3 \int_0^{\Theta/T} \tau(x) \frac{x^4 e^x}{(e^x - 1)^2} dx \qquad \text{Eq. 10}$$

Where Θ is the Debye temperature. Finally, the evaluation of thermal conductivity is reduced to seeking a proper choice of relaxation time of phonon modes.

2.6.2.2 The relaxation time and Matthiessens' rule

The relaxation time is interpreted as the mean time a phonon spends in a particular mode. Its evaluation falls within the standard category of transition rates in which the Fermi's Golden Rule is used. Various scattering mechanisms are discussed in the following section. When there is more than one scattering mechanism operative, the total relaxation time is determined as:

$$\tau^{-1} = \tau_1^{-1} + \tau_2^{-1} + \tau_3^{-1} + \cdots \qquad \text{Eq. 11}$$

This is the Matthiessens' rule which is the mathematical expression that scattering rates (= 1/τ) are *additive*. There is no strict justification of the rule. The two important assumptions behind the rule are first, the different scattering events are independent. Secondly, the scatterings events are infrequent in the sense that only seldom do two scattering events happen at the same time and the occupation factor does not fluctuate much with time. These three assumptions are quite well satisfied in the phonon dynamics in solid state.

2.6.2.3 Callaway's model

The application of the Eq. 10 with a specific set of scattering events including surface diffusive, phonon electron, umklapp phonon and defect is called the Callaway's model.[15] The relaxation rate is:

$$\tau^{-1} = \tau_{surface}^{-1} + \tau_{electron}^{-1} + \tau_{umklapp}^{-1} + \tau_{defect}^{-1} \qquad \text{Eq. 12}$$

The proper form of each relaxation time is discussed in the following section. The Callaway's model is a two way machine: you may extract the phonon scattering rates and relaxation times from the thermal conductivity, or you may obtain the thermal conductivity given the scattering rates. The model has found great success in bulk semiconductor such as GaAs and Si.

2.6.2.4 Relaxation times for various scattering mechanisms

2.6.2.4.1 Diffusive surface scattering

The diffusive surface scattering relaxation time is $\tau_{surf}^{-1} = c / \Lambda_{surf}$, where Λ_{surf} is the surface scattering mean free path that depends mainly on geometry with correction from the finite length and surface quality of the beam. The scattering rate is taken to be independent of temperature and frequency. In bulk material, it is often the most important scattering mechanism below 4 K.

2.6.2.4.2 Phonon electron scattering

In bulk semiconductor crystals, reduction of lattice thermal conductivity due to phonon scattering from conduction electron and dopant is well known to depend on both the carrier concentration and dopant species. The phonon electron scattering mean free path has been given by Ziman as: [16]

$$\Lambda_q^{-1} = [(m^*)^2 E_{def}^2 \nu]/[2\pi\rho c^2 \hbar^3] \qquad \text{Eq. 13}$$

where m^* is the effective mass, E_{def} the deformation potential energy, ν the frequency and c the velocity of phonon, and ρ the mass density of the material. We note that the corresponding relaxation time is directly proportional to the frequency of phonon. This is the basic formula adopted in this analysis.

Finally, there is also discussion on enhancement of electron-acoustic-phonon interaction in confined geometry. Enhancement is a result of change in the spatial profile and group velocity of the phonons due to confinement. As much as 200% increase in relaxation rate from bulk value is predicted for 3×6 nm^2 cross section beam.

2.6.2.4.3 Umklapp phonon scattering

Phonon-phonon scattering is an important phenomenon for which the relaxation time approximation is not totally valid and gives us insight into the relation between scattering and thermal resistance. Phonon-phonon scattering arises from the anharmonicity of the lattice. There are two kinds of phonon-phonon scattering: *normal* and *Umklapp*. In the normal case, like scattering between two real particles, the total momentum of the phonons is conserved. In the Umklapp case, however, only the *crystal momentum* is conserved, i.e., the momentum before and after the scattering are different by a reciprocal lattice vector.

The important difference between normal and Umklapp processes is that normal processes do *not* contribute to thermal resistance. This is because the thermal conductance(Eq. 3) remains constant after scattering. The forward flow of heat energy before and after the scattering is constant despite change in number of phonons. This implies that normal processes alone cannot restore the occupation factor to thermal equilibrium value. Thus, the relaxation time approximation does not apply to the normal process. Although normal process does not directly reduce thermal conduction, they affect thermal conduction by redistributing the phonon population.

Umklapp process does contribute to the thermal resistance. The associated relaxation time is:[17]

$$\tau_{umk}^{-1} \propto v^{\alpha} T^{\beta} e^{-(\Theta_D / bT)} \qquad \text{Eq. 14}$$

where v is the frequency and θ_D the Debye temperature. The constants are $\alpha \sim 2$, $\beta \sim 1$ and $b \sim 2$. It is noted that the constants are not uniquely determined for different experiments even on the same material. Since we are not interested in the high (room and above) temperature conductivity, the exact values of the constants are not particularly vital. Since the final state of the phonon wave vector has to be out of the first Brillouin zone in order to become an Umklapp process, only high frequency \ energy phonons can participate in the process. At low temperature ($T << \theta_D$; i.e., < 50 K for GaAs), Umklapp processes are effectively “frozen out ” and no longer contribute to thermal resistance.

2.6.2.4.4 Defect scattering

Imperfection in the crystal scatters phonon by local alternation of strain and mass density. There are various kinds of defect centers including isotopic impurities, substutional impurities (eg. dopant and dissolved gas), and point, line and other lattice imperfections. The mass difference scattering at point defect results in a phonon mean free path as $\Lambda^{-1} = [4\pi D^2]/[N_i(\delta M)^2 k^4$, where N_i is the volume density of defect and δM the mass difference. The inverse 4th power dependence of k is the characteristic of Raleigh scattering from objects smaller than the phonon wavelength. Different power laws are obtained for extended defects such as screw dislocations and stacking faults. The relaxation time for point defect scattering is expressed as:

$$\tau_{def}^{-1} = \frac{a^3 w^4}{4\pi c^3} F(\frac{\Delta M}{M})^2 \qquad \text{Eq. 15}$$

where a is the linear dimension of a defect and F the atomic fraction of defect. The only known defect in the device considered here is the different Ga isotopes (60% Ga_{71} and 40% Ga_{69}) and dopants in the bi-layer beams. The MBE grown GaAs wafer is of rather high quality and relatively defect free. However, defects can be introduced during the fabrication particularly by the chemically assisted ion etch. Moreover, strain can be produced during the suspension of the device. Also, dissolved gas may be important given the large surface to volume ratio of the nanostructure. Finally, defect scattering is the most strongly affected by phonon confinement because of its strong dependence on group velocity.

2.6.3 Callaway analysis of the device thermal conductance

We may now apply the Callaway's analysis to evaluate the thermal conductance of the bi-layer and undoped beam. We fit the model to the effective thermal conductivity and plot the result in Fig. 13. We apply only diffusive surface scattering and phonon-phonon scattering to the undoped beam and all four scattering mechanisms to the bi-layer beam. The fitting parameters obtained are the relaxation time (τ) of respective mechanisms which are plotted in Fig. 14. In the following the discussion, we will also refer to the *scattering rate* ($= 1/\tau$) and scattering limited mean free path ($= c/\tau$) of the phonons (Fig. 15). The fitting parameters are listed in the Table 1.

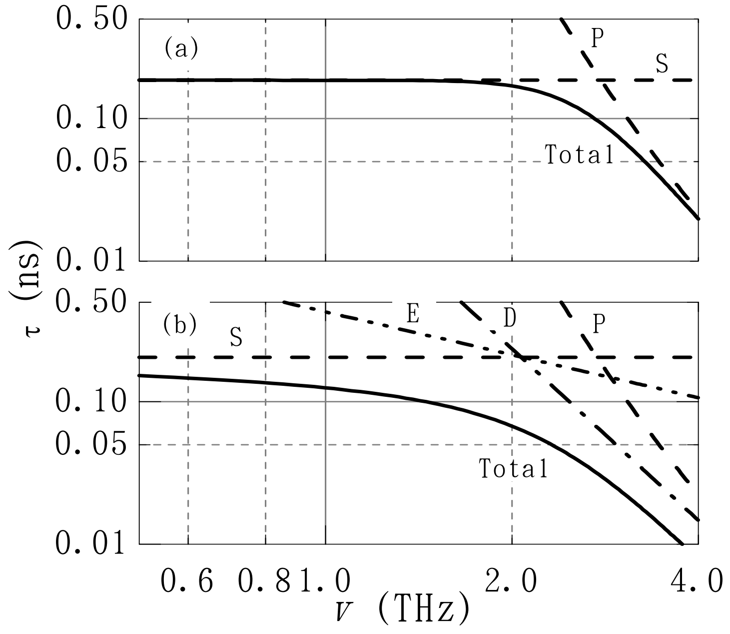

Fig. 14 The phonon scattering relaxation times (τ) (a) the undoped beam and (b) the bi-layer beam. P stands for phonon-phonon scattering, S for diffusive surface scattering, E for phonon electron scattering and D for defect scattering. The temperature or phonon-phonon scattering is taken as that of the majority of the phonons: i.e., *4 kT = h f*.

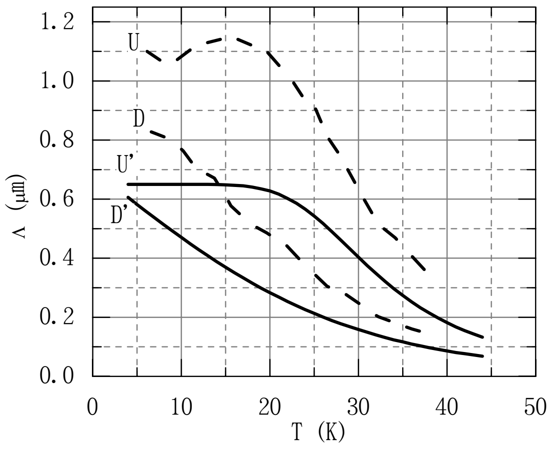

Fig. 15 Mean free path of phonons vs temperature obtained from two different analyses, for undoped and bi-layer beams. Curve *U* is for undoped beams and *D* for bi-layer beams, respectively, by the diffusive transport formula. Curve *U'* is for undoped beams and *D'* for bi-layer beams by the Callaway model. In the Callway model, the MFP is averaged across the thermal phonon population.

Beam	Scattering	Form of τ	Fitting parameter
Undoped	Surface	c/Λ	$\Lambda=0.65\mu m$
	Phonon-phonon	$Cf^2Te^{-\Theta/3T}$	$C=6.510^{-16}$ s/K
Bi-layer	Surface	c/Λ	$\Lambda=0.72\mu m$
	Electron-phonon	Af	$A=3.23\ 10^{-26}$
	Defect	Bf^4	$B=2.65\ 10^{-40}\ s^3$

Table 1 The fitting parameter for the Callaway analysis

To investigate the quality of the fit one has to look into the way how the Callaway's model distinguishes different scattering mechanisms. The statistical variance of the fit is very small (the difference between the fit value and experimental value is ~ 5 %), as one may expect when you apply a four parameter fit to a relatively simple curve. The important issue is whether it is possible to obtain a fit of same excellence while simultaneously adjusting two or more parameters. The ability of the Callaway's model to distinguish different scattering processes lies in the fact the different scattering terms have very different dependence on temperature and frequency, i.e., the fitting parameters are uniquely determined by data in a specific temperature range. By applying the model to evaluate the measured thermal conductivity of the undoped beam below 15 K, we can uniquely determine the surface diffusive relaxation time (no other scattering is significant in this regime). We then extend the fit to over 15 K to determine the phonon-phonon scattering rate. For the bi-layer beam, data between 4 to 10 K determine the surface scattering rate. The data between 10 to 15 K determine the phonon electron scattering rate. If we assume phonon-phonon scattering rates are the same in the bi-layer and the undoped beam, the data above 20 K would uniquely determine the defect scattering rate (It is in general very hard to distinguish the defect scattering from phonon-phonon scattering without conductance data up to room temperature). To conclude, we believe our analysis using Callaway's model uniquely identifies and evaluates the various phonon scattering rates in our nanoscale beams.

2.7 Discussion

2.7.1 Phonon scattering in nanostructures

The unambiguous conclusion of the experiment is that phonon scattering is much stronger in nanoscale beam than in bulk material as is obvious from its 3 orders of magnitude less thermal conductivity. Much of it comes from the strong diffusive surface scattering in the nanoscale beam. The Callaway's model enables us to study the strength of individual scattering mechanisms.

2.7.1.1 Diffusive surface phonon scattering

Below 20 K, the phonon thermal conductance of the undoped beam displays an approximate T^3 power law. In the framework of the Callaway analysis, this suggests a phonon relaxation time that is independent of frequency and temperature. This constant MFP implied is generally understood to be related to diffuse scattering at the surface and is dependent on the geometry of the sample. We note that the longest phonon MFP estimated from the data ($\approx$ 1.1 μm by the diffusive transport formula) is much shorter than the length of the beams (6 μm). Thus, at the temperature of these experiments, there is minimal possibility for ballistic transport along the length of the beams. The surface quality of the beams can be estimated from the specularity parameter $p = [(\Lambda / \Lambda_o) - 1]/[(\Lambda / \Lambda_o) + 1]$.[18] Here, $\Lambda_o = 1.12(d_1 d_2)^{1/2}$ is the MFP in the limit of completely diffuse surface scattering for a rectangular beam of sides d_1 and d_2. For our beams, Λ_o is 0.2 μm. Hence, from the phonon MFP obtained at 4 K, p is ≈0.7, indicating that phonon surface scattering is only partially specular; i.e., on average, each phonon is specularly reflected only $1/(1-p) \sim 3$ times before being diffusely scattered. This is comparable to the finding of Tighe *et al.* and is somewhat surprising. The topology of the surfaces suggests a roughness only of order 4 nm, which is likely induced by the CAIBE (chemical assisted ion beam etching) process. By comparison, the thermal phonon wavelength at our lowest temperature exceeds 10nm. Moreover, polished surfaces of macroscopic crystal used in other experiments have been shown to have a much higher specularity (~0.99). The mechanisms controlling surface specularity in nanostructures clearly warrant further investigation.

2.7.1.2 Phonon-phonon scattering

At higher temperatures, from 20 to 40K, the conductivity of both the bi-layer and undoped beams falls far below values extrapolated from the T^3 power law found below 20K. According to the Callaway analysis, this must arise from a reduction in the MFP corresponding to an increase in scattering. This phenomenon is very common in bulk crystals beyond 10 - 15 K when Umklapp phonon-phonon processes become dominant. In our mesoscopic beams, however, diffuse surface scattering is so strong that the relative contribution due to phonon-phonon scattering remains insignificant until much higher temperatures (> 40K). Surprisingly, the phonon-phonon scattering rate, deduced from the curve fitting of the Callaway analysis, is approximately 10 times higher than corresponding bulk values.

There are two possible reasons that may account for the high scattering rates that we have deduced. First, the T^3 power law obtained from the Callaway analysis is based on the Debye phonon density of state (DOS) and a constant phonon group velocity. A realistic dispersion relation of GaAs, however, shows that between 1.5 and 2.5 THz, the phonon DOS is higher than the Debye values. Correspondingly, the phonon group velocity is much smaller than that of the low frequency phonons. On the other hand, above 3 THz, the actual phonon DOS is much smaller than the Debye values. The reduction of group velocity reduces the phonon "flow rate" while the reduction of the DOS reduces the density of thermal energy carriers. Both contribute directly to a lower thermal conduction. Taking the realistic dispersion relation into account, a simplified model provides a conductivity value at 40K that is 25% smaller than that obtained using the Debye DOS and constant group velocity. We note that such an argument, while also applicable to bulk crystals, is seldom used. This is because the temperature dependence of the bulk thermal conductivity is dominated by Umklapp scattering in the temperature range where this is relevant (>30K).

The second reason for the high phonon scattering rate that is deduced may arise from surface scattering of high frequency phonons. While diffuse surface scattering is generally assumed to be frequency independent in the Callaway analysis, it is quite possible that phonons of higher frequency are scattered more effectively when their wavelengths approach the scale of surface roughness (< 4nm). In this case, the surface specularity parameter for phonons would become further reduced at higher temperatures. If diffuse surface scattering is assumed to be dominant even at 40K, the average number of specular reflection would decrease to ~1.

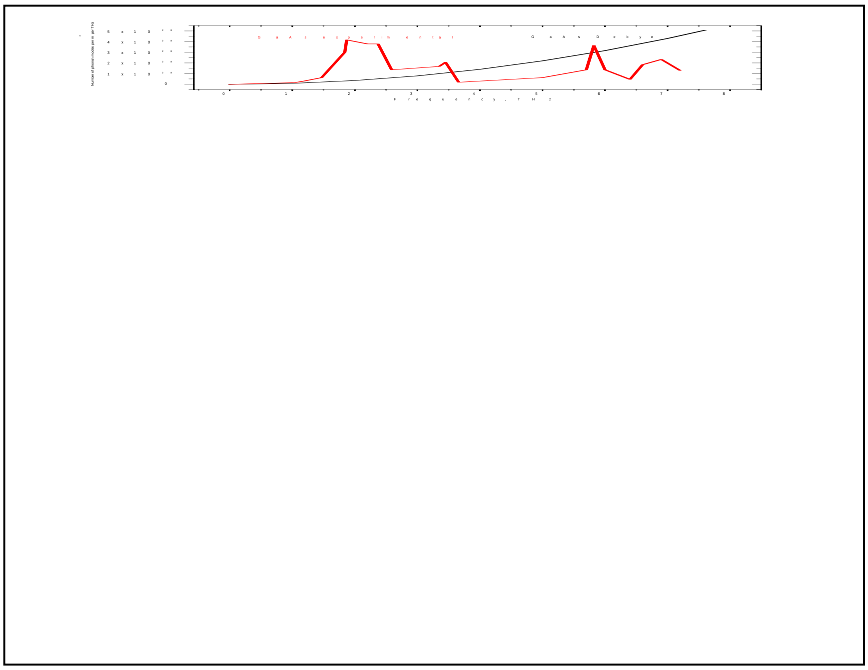

Fig. 16 The experimental and Debye phonon density of states of GaAs

2.7.1.3 Phonon electron and defect scattering

The analysis above applies equally well to the bi-layer and undoped beams. However, the data show that from 4 – 40K the bi-layer beams transport heat less efficiently than the undoped beams. This is evident from both the effective thermal conductivity and MFP's in Fig. 13 and Fig. 15. This appears to indicate that dopants on the top layer of the bi-layer beams introduce additional, efficient mechanisms for phonon scattering. There are three new components that can be identified: scattering of phonons by mobile electrons, by electrons in donor states and by point defects. The latter occurs due to the mass difference between dopants and host atoms. However, the relaxation rates we deduce from the Callaway analysis require an apparent defect density that is ~16 times higher than the known dopant concentration in our heterostructures. Additionally we deduce a phonon-electron scattering rate in our samples that is almost two orders of magnitude higher than that found in macroscopic crystals or obtained from simple models for phonon-electron scattering. The presence of dopants provides extraordinarily strong phonon scattering in nanostructures that requires further investigation.

2.7.2 Heat conduction by diffusion of hot electrons

There remains an issue critical to the validity of the measurement. The phonon thermal conductance is measured assuming that most of the heat generated in the heater is converted into phonons and transferred out of the device to the substrate through the lattice. However, there is an alternative route for the heat generated to be diffused out of the device as hot electrons through the transducer. Here, we estimate this residual effect.

The electron-phonon conductance is known as:

$$P = \Sigma(T_e^5 - T_p^5) \qquad \text{Eq. 16}$$
$$\Sigma = \frac{\hbar}{2\rho v_s}(\frac{2E_F}{3})^2 \frac{D(E_F)k_B^5\Gamma(5)\zeta(5)}{2\pi\hbar^5 v_s^3 v_F}$$

Where E_F is the deformation potential and D is the electron density of states. For GaAs heater used in the experiment, we find that $\Sigma \approx 10^{-11}$ WK^{-5}. On the other hand, the electronic heat diffusion follows the Wiedmann-Franz law as:

$$P = A(T_e^2 + T_p^2) \qquad \text{Eq. 17}$$
$$A = L / R$$

Where L is the Lorenz number. For our device where the sheet resistance per square is ~ 200 Ω, $A \approx 5 \times 10^{-12}$ WK^{-2}. We can now put together Eq. 16 and Eq. 17 to solve for the distribution of heat. Some results that are practical to the measurement are shown in Table 2.

T	Power	T_e	T_{ph}	Heat to phonon	Heat to electron	% to electron
10 K	106.7 nW	21 K	11.8K	105 nW	1.7 nW	2%
4 K	16.6 nW	12 K	6.1K	16 nW	0.6 nW	4 %

Table 2 Heat dissipation in the GaAs heater

We therefore conclude that most of the heat goes into the phonon modes.

2.7.3 Temperature gradient and thermal flux across different beams

In the analysis, we extract thermal conductance of a bi-layer beam as a quarter of the conductance of the 4 beam device. This assumes that heat flows evenly in all 4 beams. This may not be a valid assumption since the heater is not in the middle of the device. There is a similar question regarding whether the thermometer is measuring the temperatures of the ends of the beams.

We answer these questions by carrying out a finite element simulation of heat transport of the device to see the distribution of heat flow and whether there is a temperature gradient across the cavity. The first model has a symmetric heater and thermometer located at the center of the device. The second one mimics the real device with asymmetric heater and thermometer. The heater and thermometer have the shape of a polygon instead of the meanders to simplify the simulation. The models are shown in Fig. 17. The simulation result is shown in Table 1

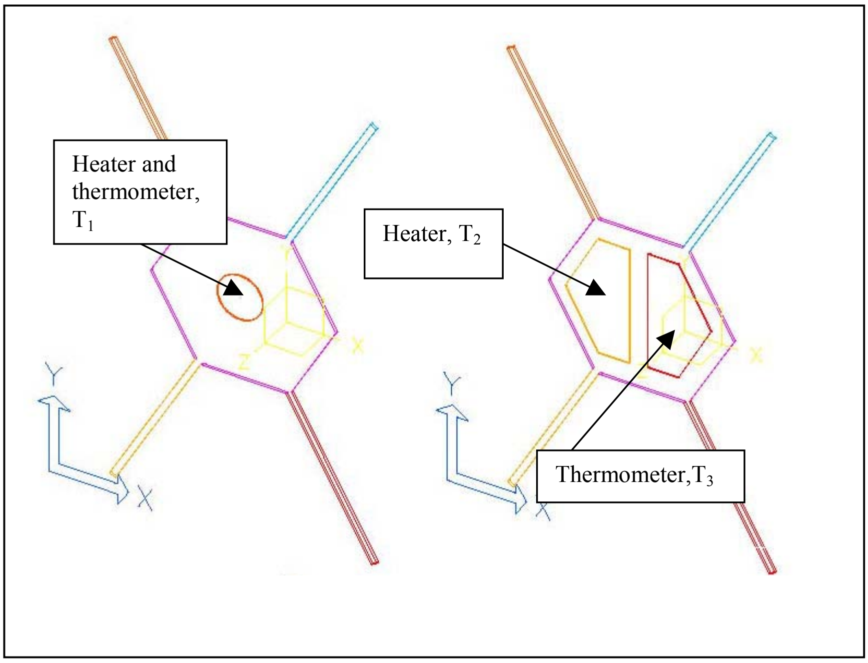

Fig. 17 The finite element models for temperature gradient simulation

.

Simulation input		Simulation result					
		T (symmetric model)	T (asymmetric model)		Thermal conductance, nWK^{-1}		
T, K	P, nW	T_1, K	T_2, K	T_3, K	symmetric model	asymmetric model	theoretical values
4	1.5	4.28	4.23	4.22	5.4	6.8	6.5
4	4	4.71	4.60	4.60	5.6	6.6	7.3
4	8	5.27	5.10	5.09	6.3	7.3	8.0

Table 3 Result of finite element simulation

The simulation indicates that the effect of thermal gradient in the cavity is very limited. First, compare the phonon temperatures at the heater, T_2, and at the thermometer, T_3, of the asymmetric model. They do not result in a significant difference and therefore the temperature measured by the thermometer can well represent the temperature of the cavity. Next, compare the thermal conductance computed from the thermometer temperature of the asymmetric model and the theoretical values input to the simulation of the beam. The first one is the combined resistance due to both the legs and the cavity. Nevertheless, they agree with each other within 10%. This indicates that the thermal resistance of the cavity is much smaller than that of the legs. Finally, we conclude the measurement is valid as the thermal conductance of the legs regarding the geometry of the device.

2.8 Conclusion

We report detailed thermal conductance measurements on suspended GaAs nanostructures and determine the effective thermal conductivity of bi-layer and undoped mesoscopic beams from the data obtained. We determine that from 4 – 40K diffuse surface scattering plays a major role in phonon transport within nanostructures. The surface specularity of the beams studied appears to be rather low. The presence of dopants is found to have an unexpectedly strong effect on the scattering of phonons. We provide a quantitative estimate of important phonon scattering processes that are operative, and find that many of them (surface, defect and mobile electron scattering) are far more effective in mesoscopic beams than in a bulk crystal.

3 Nanoscale calorimetry: Phonon density of state and heat capacity measurement

3.1 Introduction

Much of the novel nanoscale phonon physics, such as the universal thermal conductance, arises from the specific phonon density of state (DOS) unique to low dimensional structures. To date, much of our understanding of the phonon DOS at nanoscale comes from theoretical analysis or indirect measurement (e.g., phonon transport). Direct probing or measurement of phonon DOS is not trivial because traditional techniques, such as neutron scattering, are not applicable on nanostructure. Heat capacity measurements remain the most useful for such quest. The trivial difficulty, certainly, is associated with small heat capacity of nanostructure.[19,20] As a result, most heat capacity measurements of nanostructure are performed on a collection of the objects, such as *milligram* of single wall carbon nanotube.

In this work, we demonstrate a nanoscale calorimeter. The calorimeters are made of silicon nitride and silicon. There are multiple purposes behind this experiment. First, we wish to demonstrate a calorimeter of very high sensitivity with resolution < 1 aJ/K. The calorimeter may be used to measure the heat capacity of other nanoscale objects, such as C_{60} or protein molecules. It may also be converted into bolometer to find application in particle detection. Second, the measurement of the addendum (i.e., intrinsic heat capacity) of the calorimeters yields a lot of physics and useful engineering information. Silicon nitride (SiN) is a common material used in bolometry. The heat capacity of thin film SiN is a very useful parameter in determining the performance of a bolometer. The heat capacity of a Si membrane, on the other hand, is a probe of the crossover of phonon DOS from bulk 3D into a 2D regime.

3.2 The silicon nitride calorimeter device

3.2.1 Introduction to the device

We will use the SiN calorimeter as the prime example for my work. A device is depicted in

Fig. 18. The Si calorimeter is fabricated and measured in a similar manner. The SiN calorimeter is fabricated from low stress SiN membrane. It is crafted into a suspended square calorimeter body with sides of 25 μm and a thickness of 1000 Å. The calorimeter body is connected to the substrate through 4 SiN beam each of which is 6 μm long and 0.2 μm wide. At the center of the calorimeter body are a gold heater and a GeAu thermometer. They are connected to the substrate through superconducting Nb leads. In the following sections, we discuss the individual components in detail.

3.2.2 The SiN calorimeter body

The SiN contributes most to the phonon heat capacity because of the relatively large volume. The material is amorphous in nature. As a result, it has extra low frequency degree of freedom and low temperature heat capacity coming from the motional tunneling states of the ions.

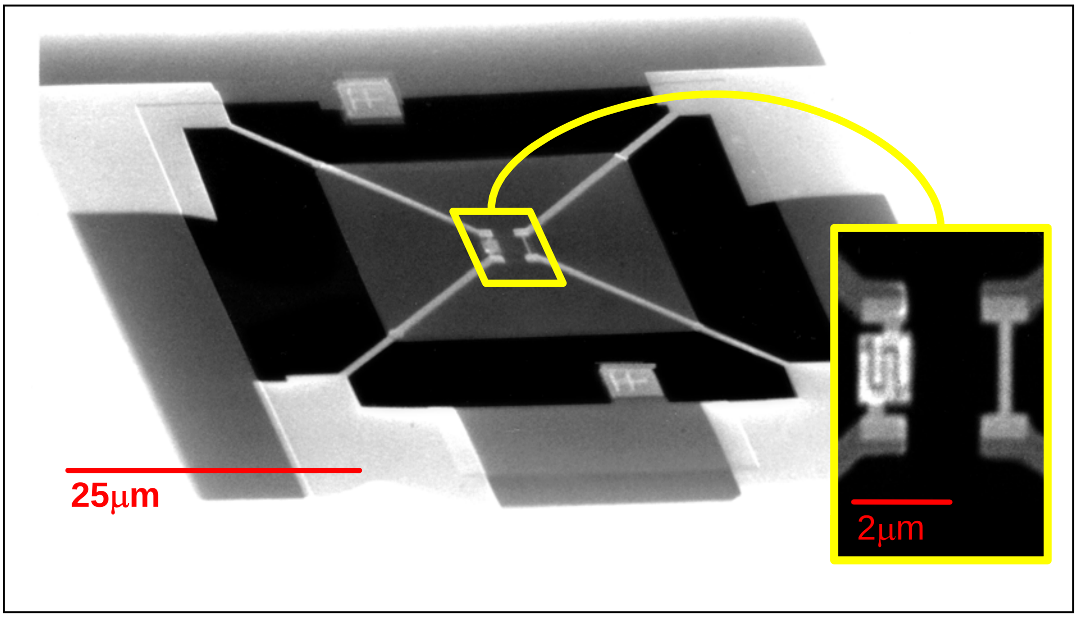

Fig. 18 The SiN calorimeter. The inset shows zoom in of the thermometer (left) and heater (right).

3.2.3 The Nb leads

The use of superoconducting Nb lead is highly advantageous over normal metal. First, well below the superconducting transition temperature (T_C ~ 8 K for Nb), the electronic heat capacity diminishes. This is especially important below 1 K when the electronic heat capacity dominates. Secondly, in the superconducting state, the cooper pairs do not carry thermal energy. Thus, there is no heat leak through electronic heat diffusion. This provides two positive impacts on the experiment. On one hand, it forces all the heat generated in the gold heater to be converted into phonons and eliminate the residual heat loss through electronic diffusion. On the other, it reduces the overall thermal conductance of the beams, increasing the thermal relaxation time and reducing the bandwidth of the measurement. Thirdly, the superconducting leads do not dissipate electrical energy. Thus, they are lossless and all the power going down the circuit is dissipated only in the heater and the thermometer.

One may note that the advantages are less significant at higher temperature, when electronic heat capacity and thermal conduction of normal metal are small, too. Thus, for temperature over 8 K, it is possible to replace the Nb leads by Au leads.

The fabrication of nanoscale Nb circuit is not trivial. If conventional ebeam lithography with PMMA resist mask is used, the Nb deposited is too contaminated to superconduct. This is because of the out-gassing of the PMMA during the sputtering process. To circumvent this problem, we use the “negative patterning technique” in which Nb is first sputtered on the whole substrate, and then the undesired part is removed to produce the Nb circuit. There is an alternative resist recipe with poly Phenylene-ether-sulfone (PES) developed for direct liftoff of Nb. However, we have found no success of such recipe in our laboratory: namely, the PES *never* sticks to the substrate.

3.2.4 The gold heater

The gold heater is fabricated to ~ 50 Ω for impedance matching purpose. The first generation of the heater, which is simply an Au wire connecting two Nb leads, shows very non-ohmic behavior at low temperature. As plotted in Fig. 19, this is because of the proximity effect which effectively turns the end of the Au heater superconducting and reduces its resistance. Because proximity effect is current dependent, it makes the heater non ohmic. Since we prefer an ohmic heater to accurately measure the heat deposited, we designed a "dog bone" shape Au heater (Fig. 20) which has widened ends of Au contact to the Nb. The proximity effect is not eliminated, but it no longer affects the overall resistance since the contribution from the ends is small.

The electronic heat capacity of gold is one of the biggest residual contributions (i.e., non phonon) to the heat capacity below 0.6 K. Thus, we fabricate a small heater using electron beam lithography to minimize its contribution. The same applies to the thermometer.

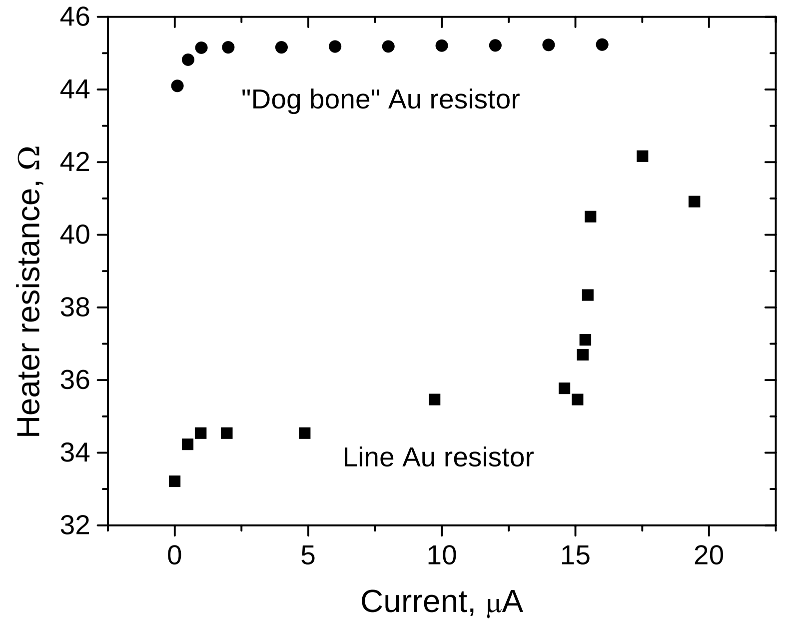

Fig. 19 The resistance versus current of (a) a line Au heater and (b) a dog bone shape heater

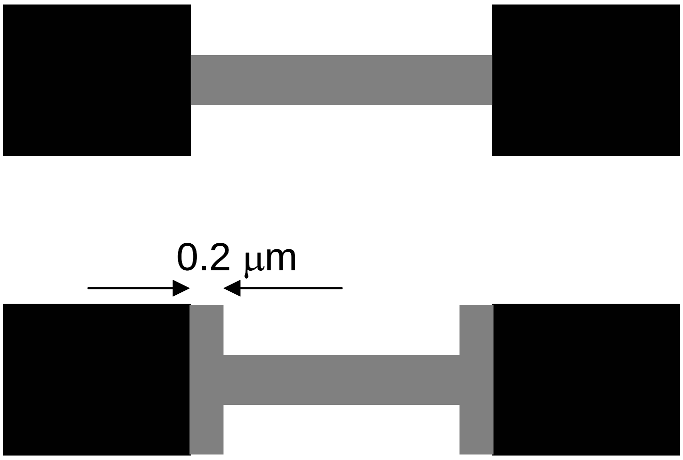

Fig. 20 The line shape (above) and dog bone shape resistor (below). Black is Nb and grey is Au.

3.2.5 The GeAu thermometer

The thermometry is a vital component to a calorimeter. The key features of the thermometer include sensitivity, bandwidth and power dissipation. The different features yield conflicting requirements. Thus, a "good" thermometer is one that could balance all the trade-off to satisfy a particular application. In our experiment, there are two important requirements that are not common in ordinary calorimetric application: First, the bandwidth of thermometry is large from 200 kHz to 1 MHz. Second, because of the small volume of the thermometer, the internal electron-phonon resistance is particularly high. The large bandwidth requirement prohibits use of high impedance (> 10 kΩ) thermometers such as superconducting tunneling junctions or some high resistance doped semiconductor thermometer unless with exotic impedance matching techniques.[21] Finally, we chose GeAu (a metal insulator transition material) because of its relatively low resistivity (~ 0.1 Ω cm), reasonable sensitivity (dR/dT / R ~ 10 % / K) and ease of fabrication.[22] Other candidates include NbSi which is too resistive and is less sensitive above 1 K.

To further reduce the resistance of the GeAu thermometer, we adopted an inter-digitated pattern of Au electrodes. The pattern effectively reduces the "number of square" of the resistor to 1/10. This allows a thermometer at ~ 5 kΩ for 500 Å thick film. The Au electrodes also enhance the electron-phonon coupling so as to increase the allowed probe current of the thermometer.

3.2.6 Detailed fabrication procedure of SiN calorimeter

a. Preparation of SiN membrane

- The 1000 Å thick SiN substrate is obtained from Berkeley fabrication facility through MEMS exchange. By optical lithography, we pattern on the back side (unpolished side) of squares with side = 750 µm. The length of the square at the back side (L) is related to the side of the membrane (l) and the thickness of the wafer as (L-l) ~ 1.33t.
- The back side square is etched by RIE.
- A KOH solution is prepared by 200 g of KOH in 400mL of water and heated to 85°C. The wafer is etched in the KOH solution for 6 ½ hrs. The membranes are ready when they are transparent to light from the back side.

b. Ebeam lithography of alignment marks

- The Design CAD file of the device is HC13.dc2.
- With standard ebeam lithographic technique mentioned in section, we deposit gold alignment mark of 500Å thick.

c. Ebeam lithography of gold heater and thermometer electrodes

- The gold heater and thermometer electrodes are also defined by ebeam lithography. The thickness of the Cr adhesion layer is 30 Å and the Au layer is 220 Å. The thickness has to be pretty exact to produce the desired resistance of the heater at 50 Ω

d. GeAu thermometer deposition

- The GeAu thermometer pattern is also defined by electron beam lithography. After developing the resist, the chip is ion milled for 3 s (at 500V and 20 mA beam current) to provide a clean contact.
- The GeAu is formed by alternative deposition of Ge and Au. The Ge thickness is 40 Å and the Au thickness is 10 Å. The first and last layers are both Ge so that all Au layer are sandwiched between Ge layer. The total number of Ge layer is 13 and that of Au is 12.

e. Protective SiO_2 layer

- A protective layer of 300 Å thick silicon dioxide is deposited over the heater and thermometer to protect it from future plasma etching

f. Nb deposition

- The Nb is deposited onto the whole substrate (no resist mask)
- The Nb sputtering chamber must have very high vacuum ($< 10^{-7}$ Torr). Before the deposition, extended pumping (> 7 hrs) is needed. The substrate is ion milled for 3 s to provide good contact.
- DC sputtering is used. On a 2” target, the sputtering gun is current regulated at 0.8 A. At an Ar plasma pressure of 0.8 mT, the voltage is ~ 200V. The

sputtering rate is ~ 15 Å/s, the sputtering time is 28 s.

g. SiO_2 Nb etching mask

- A SiO_2 mask is deposited for the following Nb etch. Silicon dioxide is used because it is an electrical insulator
- The mask pattern is defined by ebeam lithography. The mask thickness is 500 Å.

h. Ti finger pad mask

- The finger pad mask is defined by optical lithography.

i. Nb etch

- The Nb etch is done in the electron cyclotron resonance (ECR) plasma etcher. The plasma power is 300 W. The DC bias is -200V. Chlorine gas is flowed into the chamber at 5 sccm to keep a chamber pressure of 3 mT. The etch takes ~ 10 s.

j. SiO_2 calorimeter body mask

- The calorimeter body mask is 1000 Å thick SiO_2.

k. SiN etch

- The SiN etch is done in the electron cyclotron resonance (ECR) plasma etcher. The plasma power is 300 W. The DC bias is -100V. NF_3 gas is flowed into the chamber at 5 sccm to keep a chamber pressure of 3 mT. The etch takes ~ 60 s.

3.3 The phonon physics and heat capacity of nanoscale calorimeter

We would discuss the physics of phonon including the density of state and heat capacity in this section. This knowledge is very important for us to figure out the appropriate setup for the measurement.

3.3.1 The phonon Debye heat capacity

The well known Debye 3D (bulk) equation of phonon heat capacity is:

$$C_{3D} = \frac{2k_B^4 V T^3 \pi^2}{5\hbar^3 c^3} \qquad \text{Eq. 18}$$

We note that the only physical characteristic of material that is relevant is the velocity of sound. This is often represented as the Debye temperature, $\theta_D = 2\pi\hbar c(3N/4\pi V)^{1/3}$. A soft material, such GaAs, has a small Deybe temperature (Θ_D = 345 K for GaAs), small sound velocity and a large phonon heat capacity. On the other hand, a hard material, such as diamond, has a large Debye temperature (Θ_D = 2230 K for diamond). The Debye temperature of Si is 640 K.

The Debye temperature of SiN is not well known. This is because it is a thin film material for which the bulk heat capacity is not measured. But we could estimate the velocity of sound from the Young's modulus and Poisson ratio. For SiN, E = 300 GPa, $\nu = 0.25$ and $\rho = 3000$ kg / m^3. The relevant elastic modulus are $C_{11} = E\ (1-\nu)/\ (1+\nu)\ (1-2\nu)$ and $C_{44} = E\ /\ (1+\nu)$. Finally, the velocities of sound are $c_l = (C_{11}/\rho)^{1/2} = 10954$ m/s and $c_t = (C_{44}/\rho)^{1/2} = 8944$ m/s. Finally, we estimate the Debye phonon heat capacity of SiN to be $C_D = 0.58\ T^3$ μJ/Kcm^3. [23]

3.3.2 The dimensional crossover of phonon DOS in thin film

The 3D Debye phonon heat capacity works well for most geometry until the phonon wavelength becomes comparable to the dimension of the object. The dominant phonon wavelength is estimated as $\lambda = hc/4kT$ which is approximately 0.1 μm at 1 K. In a thin film, when the dominant wavelength approaches the thickness of the film, there is a transition from 3D to a 2D phonon gas. The phonon modes are no longer equally spaced in the k-space. Instead, they form sheets in the k-space. The heat capacity is evaluated as:

$$C_P = \frac{2k_B S}{2\pi}\left(\frac{k_B T}{c\hbar}\right)^2\left[\int_0^\infty \frac{x^3 e^x}{(e^x-1)^2}dx + \sum_{n=1}^{\infty}\int_{nx_o}^\infty \frac{x^3 e^x}{(e^x-1)^2}dx\right] \qquad \text{Eq. 19}$$

where S is the surface area of the thin film and $x_\circ = \pi\hbar c / k_B T l$. The first integral in the bracket corresponds to a true 2D gas:

$$C_{2D} = \frac{9k_B^3 S T^2}{\pi 2\hbar^2 c^2}(2.4) \qquad \text{Eq. 20}$$

The transition between 2D and 3D is revealed as a change of power law in heat capacity (from T^3 for 3D to T^2 for 2D). The transition point could be defined as the temperature when the 3D and 2D heat capacities are equal ($C_{3D} = C_{2D}$), the characteristic thickness of the film, *l,* is:

$$l = 0.35\pi\hbar c / k_B T \tag{Eq. 21}$$

For a 500 Å thick silicon film, this happens at ~ 0.8 K. We plot the full transition of the silicon film in Fig. 21.

3.3.3 The surface phonon modes

The Debye theory that is applied to the bulk material does not account for phonon modes in the surface (even for the 2D case). In a nanostructure when the surface area to volume ratio is large, the contribution of it to heat capacity may become significant. The surface phonon mode heat capacity is:

$$C_S = 3\pi\xi(3)\frac{k_B^3}{h^2}\frac{2c_t^4 - 3c_t^2c_l^2 + 3c_l^4}{c_t^2c_l^2(c_l^2 - c_t^2)}AT^2 \tag{Eq. 22}$$

where A is the surface area. In a smooth 2D film, the surface phonon mode heat capacity is usually only 10 to 20% of the 2D phonon gas heat capacity. In nanoclusters or film with very rough surface (large effective surface area), however, the surface modes could become the most dominant source of phonon heat capacity.

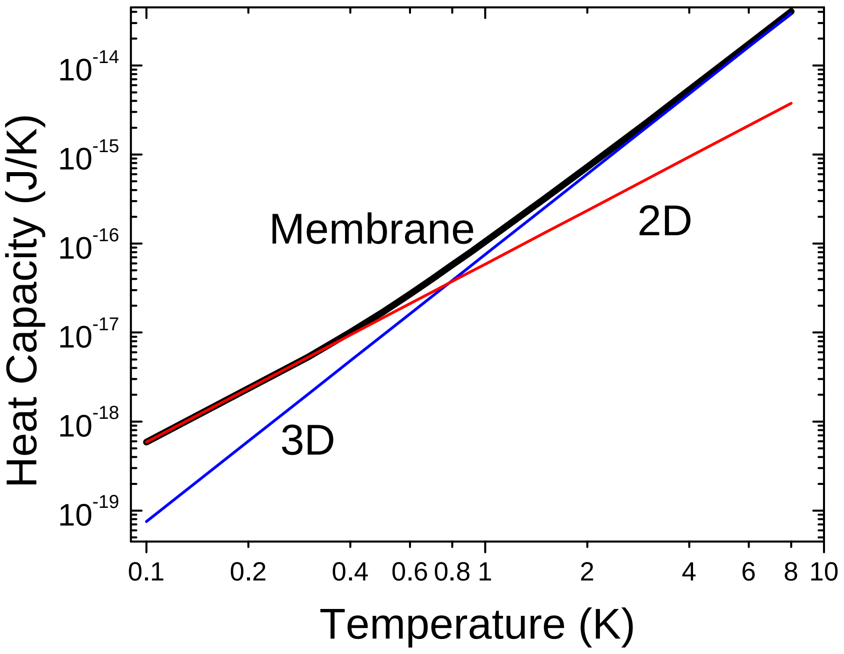

Fig. 21 The calculated phonon heat capacity of a 500 Å Si membrane (dark line) with dimensional crossover of phonon DOS at 0.8 K

3.3.4 The motional tunneling state of ion in amorphous solid

In a glassy, amorphous solid, the local motion of ion tunneling could contribute to heat capacity. There is no well developed theory for such phenomenon. One simple theory is to treat such state as two level system (TLS). We will discuss this in further detail in later section.

3.3.5 The electronic heat capacity of normal metal and superconductor

The electronic heat capacity of a normal metal is:

$$C_{el} = \frac{1}{2}\pi^2 n k_B T / T_F \qquad \text{Eq. 23}$$

where T_F is the Fermi temperature (= 6.4×10^4 K for Au). At low temperature below 1 K, because of the linear power law (as opposed to the T^3 law for phonon gas), electronic heat capacity becomes dominant. In fact, in the SiN calorimeter, the heat capacity of the gold heater and gold electrodes for the thermometer becomes as big as that of the phonon gas in the SiN, although the volume of the gold is less than 0.02% of that of the SiN. Thus, it is necessary to minimize the size of the heater and the thermometer.

This also explains why it is necessary to use superconducting Nb for electrical leads. Unlike normal metal, well below the transition temperature, the electronic heat capacity of a superconductor vanishes. This is especially important for the Si calorimeter when we try to observe the dimensional crossover in phonon DOS.

3.4 The principle of measurement

3.4.1 The pulse method of heat capacity measurement

As discussed below in detail, the equation of motion of a calorimeter is very similar to a resistor-capacitor electrical circuit. The calorimeter can be considered as “frequency doubling low pass filter”. Suppose there is a calorimeter of heat capacity *C* that is thermally connected to the environment with thermal conductance *G*, we apply a heat power with peak power *P*. Due to the finite heat capacity, the rise of the temperature of the calorimeter will take an exponential form:

$$\begin{aligned} T(t) &= T_{\circ} + \Delta T(1 - e^{-t/\tau}) \\ \Delta T &= P/G \end{aligned} \qquad \text{Eq. 24}$$

where τ is the thermal relaxation time constant. Such a trace is plotted in Fig. 22. From the plot, we could determine *G* and τ, from which we evaluate the heat capacity as:

$$C = G\tau \qquad \text{Eq. 25}$$

The pulse method is mathematically equivalent to the frequency domain method discussed in the following section. In practice, time domain measurement is usually harder to perform because a wide band measurement is needed. We would still prefer to implement it because in bolometry, time domain measurement is necessary.

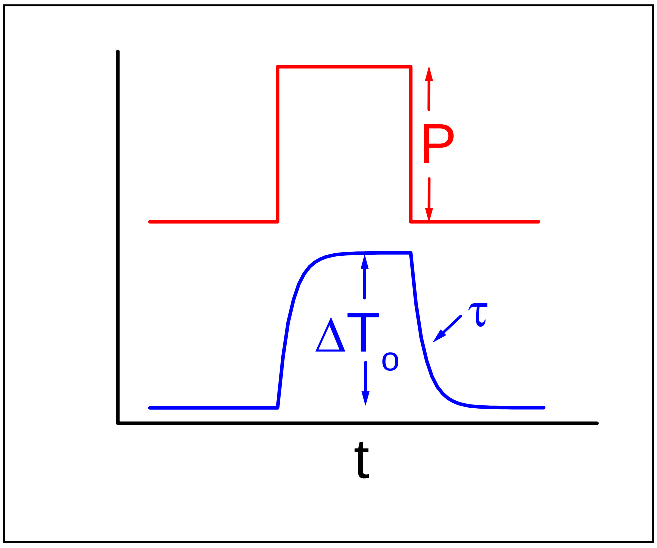

Fig. 22 The temperature response of a calorimeter to a heat pulse

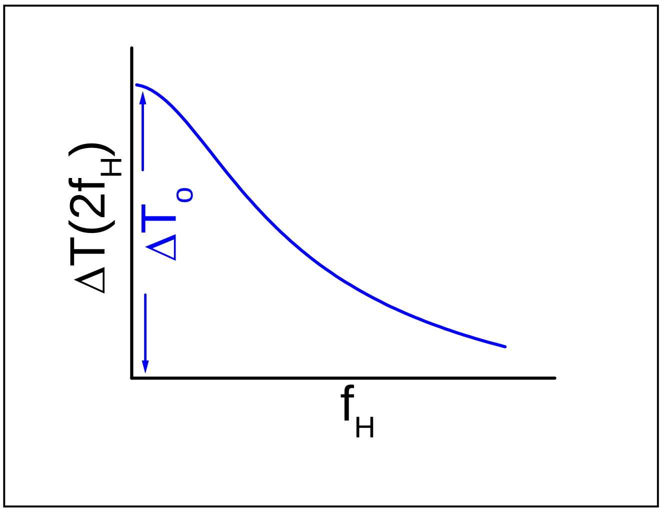

Fig. 23 The response of the calorimeter in the frequency domain

3.4.2 The frequency domain method of heat capacity measurement

In this method, we apply a sinusoidal voltage $V=V_o \sin wt$ to the heater. The response of the thermometer is:

$$T(t) = \frac{\Delta T_O / 2}{\sqrt{4\tau^2 w^2 + 1}} \sin(2wt + \Theta) + \Delta T_O / 2 \qquad \text{Eq. 26}$$

$$G = P_O / \Delta T_O$$

$$P(t) = P_O (1 - \cos 2wt)/2$$

$$\Theta = \tan^{-1}(-1/2\tau w)$$

Where $P_o = V_o^2 / R$ is the *peak* power. Note that in addition to the frequency response of the calorimeter at 2f, there is a DC response. The 2f response diminishes at high frequency, from which we could determine τ as:

$$\left(\frac{\Delta T_O}{2\Delta T(2f)}\right)^2 = 16\pi^2 \tau^2 f^2 + 1 \qquad \text{Eq. 27}$$

where ΔT(2f) is peak response at 2f as plotted in Fig. 23

3.5 The experimental method of heat capacity measurement

3.5.1 The ^{3}He cryostat

The ^{3}He cryostat used is a commercially available one from Dessert. With a impedance filled 1-K pot, it operates continuously at 1.2 K. The Helium-3 bath could be pumped to cool down to below 0.35 K for over 8 hours.

The cryostat features coaxial cable connection for high speed measurement. We tailor made a detachable sample holder on which the device (a 3mm side square die) is clamped and wire-bonded to. When cooling down the sample to 4 K, as opposed to the suggestion by the manual, exchange gas (^{3}He or ^{4}He) is not necessary. This is very important for our measurement as adsorbed film of He gas could have big contribution to the heat capacity.

3.5.2 The bandwidth of the measurement

It is important to have prior knowledge of the desired bandwidth before constructing the experimental setup. The 3-dB point of response of calorimeter is, according to Eq. 27, at frequency $f = 1 / 4 \pi \tau$. Since the frequency roll off the calorimeter is very slow, we would rather choose a bandwidth well beyond that frequency. In practice, a bandwidth $BW = 1/\tau$ would be sufficient.

The heat capacity of the calorimeter is estimated from its geometry and the SiN phonon heat capacity to be $C = 3.5 \times 10^{-17} T^3$ [J K^{-4}]. The phonon thermal conductance is estimated according to the thermal conductance measured in the previous section to be $G = 0.3 T^3$ [nWK^{-4}]. This is a conservative estimation in which underestimate the heat capacity and overestimates the thermal conductance to yield the highest possible bandwidth. As a result, $\tau = 1.2$ μs and a bandwidth of ~ 1 MHz is needed.

3.5.3 The 5 MHz bandwidth measurement setup

The key feature of the 5 MHz setup is the ability to monitor a 5 kΩ GeAu thermometer at high bandwidth. On the heater side, 50 Ω matched attenuator is used to attenuate the heater signal. This is appropriate because the heater is made to 50 Ω. On the thermometer side, we use a CL 425 op-amp from National Semiconductor. The op-amp features high input impedance at over 10 MHz and has a low intrinsic noise of 1 nV/√Hz (The actual noise is ~ 4 nV/√Hz arising mainly from the feedback resistor). Although the gain is not large (~ 10), it has an 50 Ω output that is conventional for coupling to regular RF amplifier for further amplification.

3.5.4 The 200 kHz bandwidth measurement setup

As it turns out for the SiN calorimeter experiment, we heavily underestimate the heat capacity due to the tunneling of the glassy states in the material. As a result, the thermal relaxation time of the calorimeter is much longer at 20 μs. Here, we draw in Fig. 24 the appropriate setup for measurement.

For the 200 kHz measurement, no impedance matching is needed. The attenuator used at the heater side could simply be a bias resistor (~ 10 kΩ). On the thermometer side, the DC bias current source is a DC power supply and a bias resistor (~ 100 kΩ). The amplifier used is a BJT input pre-amplifier (e.g. SR 552). Subsequently a generally pre-amplifier (e.g., SR 560) could be used to further boost up the signal.

For time domain measurement, a pulse generator is used to generate the pulse for heating. A digital oscilloscope (e.g., HP infinium 100 MHz) monitors and records the measurement. For frequency domain measurement, a signal generator is used to power the heater and a lock-in amplifier is to replace the scope for monitoring the thermometer signal. Since the detection of the thermometer signal is at twice of the heater signal, a frequency doubler can be used to generate the reference at 2f. Alternatively, some lockin (such as SR 830) could detect 2nd harmonic directly.

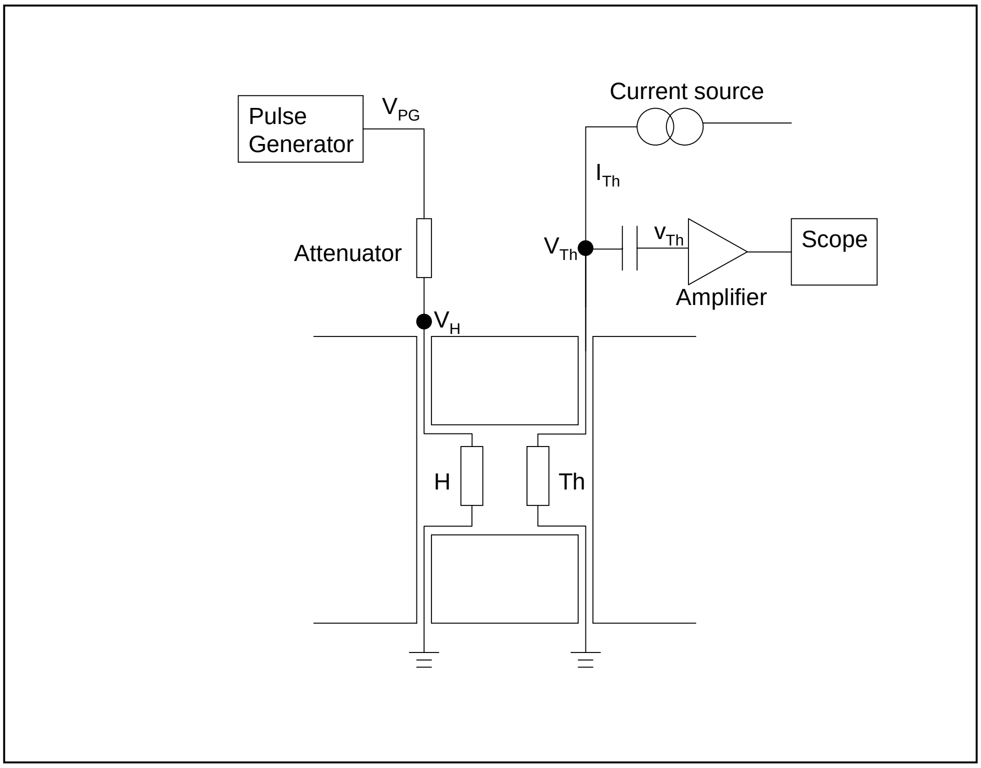

Fig. 24 The schematic for heat capacity measurement

3.6 The experimental result on SiN calorimeter

3.6.1 Introduction

In this section we demonstrate the operation of the SiN calorimeter by first measuring the heat capacity of the calorimeter itself. Next, we use it to measure the heat capacity of an adsorbed film of He gas.

3.6.2 Cooling down of the device

The device is mounted and wire bonded onto the sample holder. Then the sample holder is mounted on the cryostat and the cryostat is cooled down to 4 K with no exchange gas used. In Fig. 25, we show the resistance of the heater and thermometer (including Nb) during cooling. On the heater side, the resistance experiences a precipitous drop at ~ 7.5 K when the Nb becomes superconducting. The actual heater resistance is then measured to be 22Ω. On the other hand, the resistance of the thermometer goes up at low temperature as expected due to the metal insulator transition.

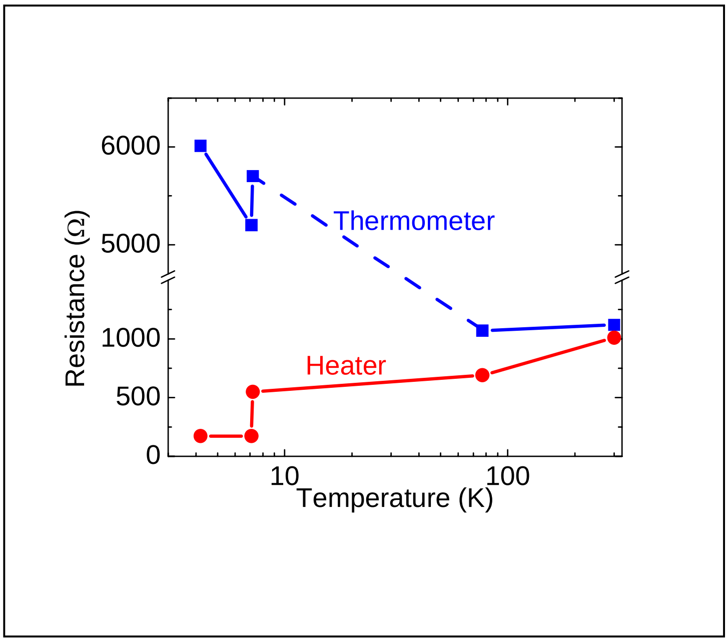

Fig. 25 The resistance of the calorimeter heater and thermometer (including Nb) during device cool down.

3.6.3 The ohmic heater

The heater gold contact to the Nb is made into a dog bone shape as discussed in section 3.2.4 to ensure ohmicity. The critical current of the Nb is > 20 μA at 4 K and is ~ 7 μA at 6.5 K.

3.6.4 The calibration of the thermometer

The GeAu thermometer is calibrated against a commercial NTD Ge thermometer on the cryostat. The temperature dependence of its resistance is shown in Fig. 26. We also see that temperature sensitivity is highly current dependent. This is because of electron-phonon decoupling which tends to keep the electron gas at higher temperature. As a result, the response becomes flat even with a very small probe of 1.5 nA below 0.5 K.

A quick analysis reveals that the hot electron effect may be due to power injection other than the bias current. The electron-phonon coupling is:

$$P = V\Sigma(T_e^5 - T_{ph}^5) \qquad \text{Eq. 28}$$

Where P is power, V is the volume and $\Sigma = 2 \times 10^9$ W/m^3 K^5. The volume of the thermometer is ~ 0.1 μm^3. Thus, the power to maintain the electron temperature at 0.5 K is ~ 5 pW. On the other hand, the thermometer bias power at 1.5 nA is only 40 fW.

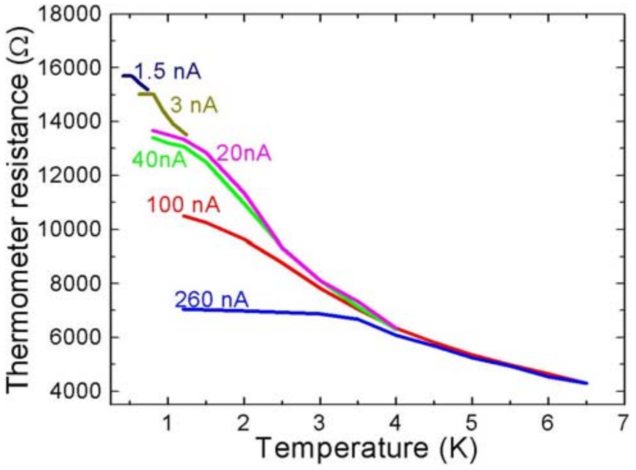

Fig. 26 The resistance of the GeAu thermometer versus temperature

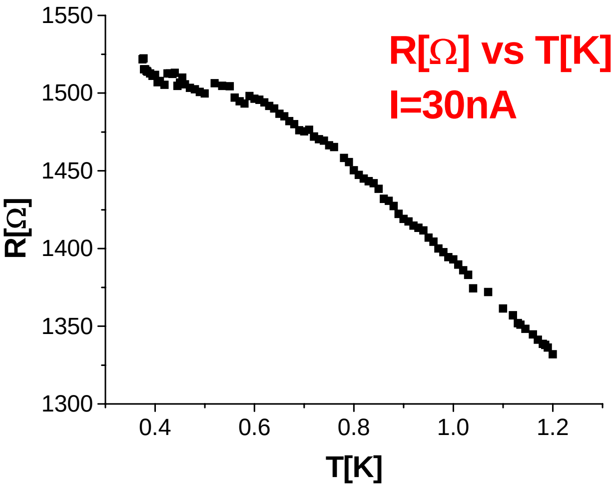

Fig. 27 The GeAu thermometer at lower temperature with chilled (4 K) bias resistor

We later realize that the power actually comes from the Johnson noise of the bias resistor at room temperature. The room temperature Johnson noise of a 100 kΩ resistor is ~ 40 nV/√Hz, which could easily inject pW of power into the thermometer. We verified this hypothesis in subsequent experiment where the bias resistor is also cooled to 4 K, and found that another GeAu thermometer would operate down to 0.4 K, as shown in Fig. 27.

3.6.5 Hopping noise in the thermometer

As discussed later in the error analysis section, hopping noise in thermometer is one of the most dominant noise sources in the thermometry. We have measured the hopping noise by observing the spectral fluctuation in resistance when the thermometer is biased by a DC current. As shown in Fig. 28, at a bias current of 200 nA, it has a hopping noise of 0.05 Ω/√Hz from 10 to 200 kHz. The noise arises because of the GeAu is a "dirty metal" material. We note that such noise is not found in the Au heater.

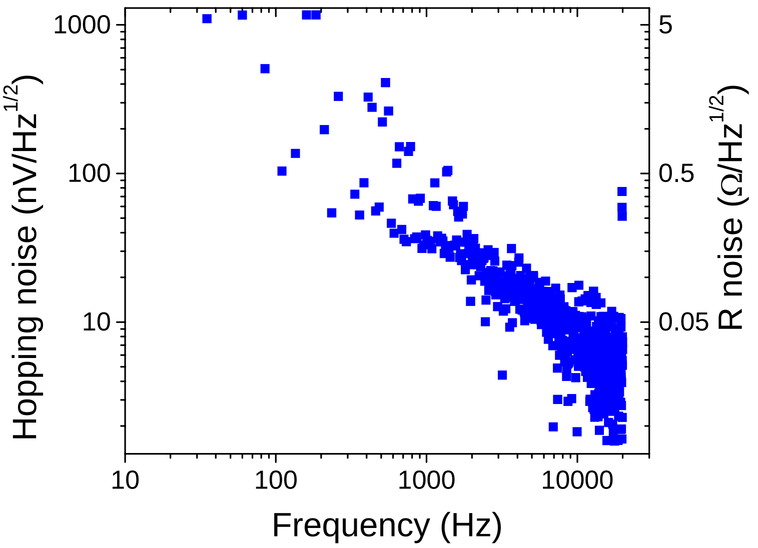

Fig. 28 The hopping noise in the GeAu thermometer biased at 200nA

3.6.6 Example of heat capacity measurement by the pulse method

In this section, we demonstrate in detail the measurement of heat capacity at 4.5 K by the pulse method. The thermometer is biased at 40 nA. Heat pulses are applied to the heater at a power of 0.125 nW, each for a period of 400 μs. The resultant temperature change of the calorimeter, is plotted in Fig. 29. From that we conclude that the temperature change is 93 mK for this starting temperature and pulse amplitude and duration. From this, we deduce the thermal conductance of the device in the steady state as $G = \dot{Q} / \Delta T = 0.125\ nW / 93\ mK = 1.34\ nW/K$. Further, we apply a least square fit to the exponential decay of the rising edge to determine that the thermal relaxation time is 18.3 μs. From this we deduce heat capacity is $C = G\tau$ =24.5 fJ/K at 4.5 K.

3.6.7 Example of heat capacity measurement by the frequency domain method

We also demonstrate the heat capacity measurement by the frequency domain method. A sinusoidal heating voltage is applied to the heater. When the frequency of the sine signal increases, the response in the thermometer rolls off.

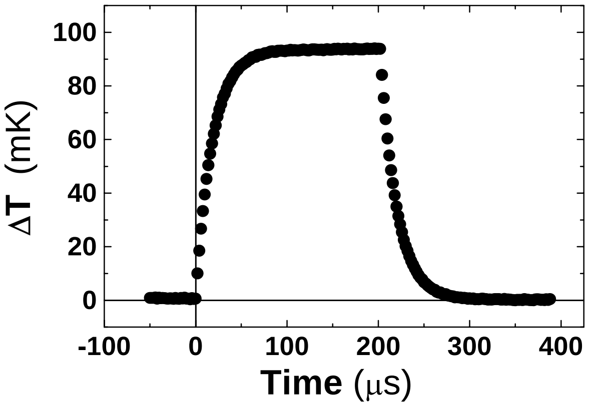

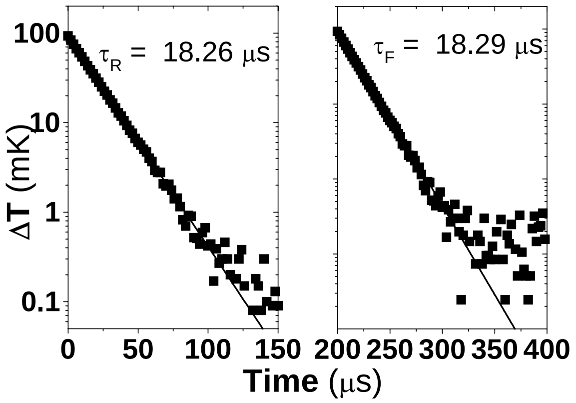

Fig. 29 The pulse response of the calorimeter in linear axis (above) and in semi-log plot (below). The data represent the average of 200 K individual pulses each separated by time 1 ms, which greatly exceeds the thermal relaxation time. Discrepancy between the rising and falling time constants arises from the temperature dependence of the thermal relaxation time. The pulse rise starts from a temperature of 4.5 K while

the falling pulse begins at 4.5 + 0.0934 = 4.5934K. We employ only the pulse rises in our analyses of heat capacity.

3.6.8 Verification of integrity of signal from the device

Before we present the experimental result in detail, we would try to look into detail whether the signal is *real*. Could the thermometer signal be just some electrical pickup between the heater line and the thermometer line? Could the exponential decay be due to the roll-off of some capacitive element in the circuit? Here we investigate the integrity of the signal by various checks.

3.6.8.1 The frequency doubling of thermometer signal

If the frequency domain measurement technique is applied to the calorimeter, we observe the thermometer response at a frequency of $2\ f$ when the heater voltage frequency is at f. This is a clear demonstration that the signal originates from the calorimeter by not any electrical pickup.

3.6.8.2 Possible roll off due to cable capacitance

A possible reason for the high frequency roll off of response from the thermometer could be due to the capacitance of coaxial cable connecting the device (at cryogenic temperature) to the room temperature preamplifier. This semi-rigid coaxial cable, which is part of the cryostat, is approximately 5 feet long and has a capacitance of 25 pF. Thus, the 3dB roll off of a 10 kΩ thermometer is ~ 300 kHz. On the other hand, the roll off the thermal response of the calorimeter with a measured relaxation time constant of 20 μs is only 8 kHz. Thus, the roll off in response is likely to come from the thermal response but not the capacitance of the cable.

We may also perform an independent test to verify this claim. Instead of a DC current, we bias the thermometer by a high frequency carrier at 100 kHz. The response is demodulated by a lock-in before it is monitored by a second lock-in. As similar to the DC bias measurement, we observe a roll off in response at 5 kHz. This proves that the roll off does not come from the capacitive effect in the circuit since the thermometer signal frequency is almost constant (100 ± 5 kHz = 95 to 105 kHz).

3.6.8.3 Possible roll off due to loss of efficiency of heater at high frequency

In this section we are concerned with the efficiency of the power delivery to the heater. Namely, whether the same rms power is deposited onto the calorimeter when the frequency is swept up. This is possible if the bias resistor or the cable connecting the signal generator to the heater do not pass high frequency signal.

A closer look at the frequency response of the calorimeter yields a method to clarify this concern. According to Eq. 26, apart from a response at $2f$ (that we usually detect), there is always a DC response due to the sinusoidal heating which is proportional to the heater power but independent of the frequency. It proves that a constant power is applied to the heater up to 100 kHz. Thus, the heater is behaving ideally up to 100 kHz.

3.6.9 The heat capacity, thermal conductance and thermal relaxation time of the SiN calorimeter

Finally, we determine the dynamic thermal response of the SiN calorimeter from 0.5 to 7 K. From the response, we determine the thermal conductance and thermal relaxation time and plot the result in Fig. 30. Finally, the heat capacity of the calorimeter is computed and plotted in Fig. 31.

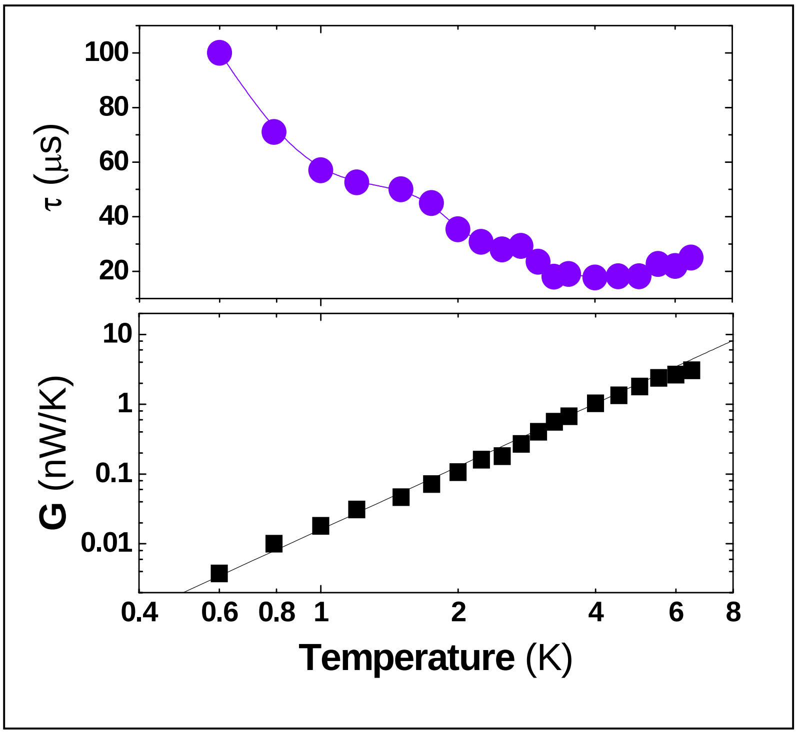

Fig. 30 The thermal relaxation time and thermal conductance of the SiN calorimeter

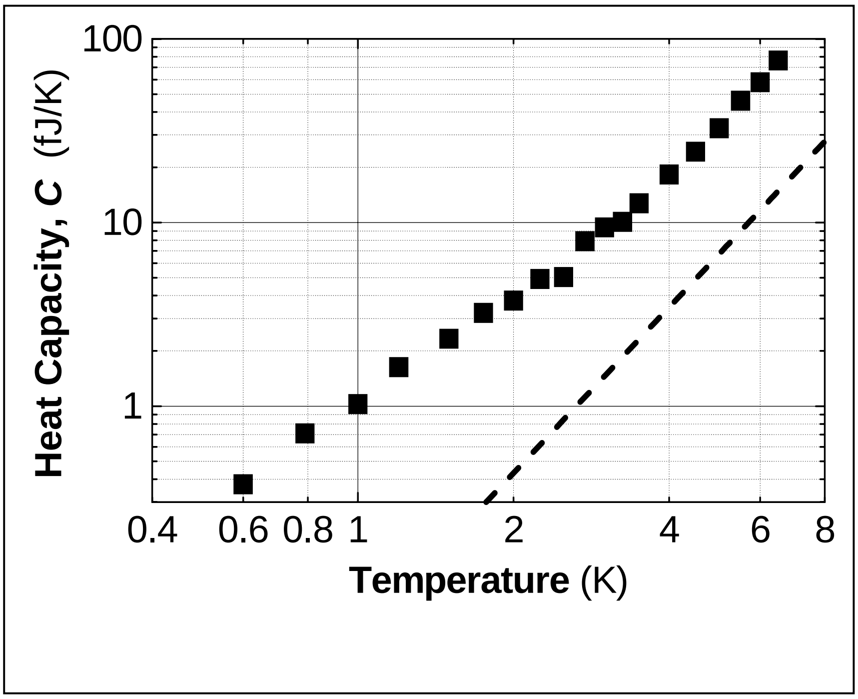

Fig. 31 The heat capacity of the SiN calorimeter

3.7 Data analysis on the SiN calorimeter

3.7.1 Analyzing the heat capacity of the SiN calorimeter

The measured heat capacity of the SiN calorimeter is plotted in Fig. 32 along with various calculated heat capacities. The measured heat capacity is apparently much higher than what is expected from the Debye phonon heat capacity. This is especially significant below 1.5 K when the heat capacity deviates significantly from the T^3 Debye law. At 0.6 K, the measured heat capacity is 20 times more than what is expected from the Debye theory.

We presume that this deviation is explained by the motional tunneling states of ions in the SiN material. Since SiN is amorphous, ions in the material could tunnel through different states. This is known to have big contribution to the heat capacity of the material particularly below 10 K.

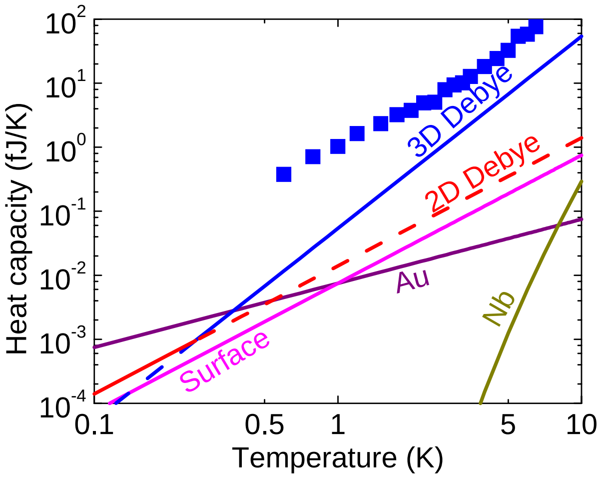

Fig. 32 The measured heat capacity of the SiN calorimeter along with evaluated heat capacity contribution from various constitutents

A simple theory is developed to estimate this contribution to heat capacity of the tunneling states. The tunneling states are modeled as two level systems (TLS) with activation energy E_k even evenly distributed between 0 to 30 K. The heat capacity of a TLS is:

$$C_V = k_B (\frac{E_K}{k_B T})^2 \frac{\exp(E_K / k_B T)}{[\exp(E_K / k_B T) + 1]^2} \qquad \text{Eq. 29}$$

Weighted over the distribution of activation energy, the average heat capacity of a TLS at 1 K is 0.05 k_B. To account for the extra heat capacity at 1K, the number of TLS in the calorimeter is (1 fJ /K) / 0.05 $k_B \approx 10^9$. Equivalently, the density of TLS in the SiN is 10^{19} cm^{-3}. This is similar to result observed in vitreous silica and the glassy tunneling states are a very probable source for the extra heat capacity.[24]

3.7.2 Analyzing the thermal conductance and relaxation thermal time constant of the SiN calorimeter

We discuss briefly the thermal conductance of the SiN \ Nb beam. Estimated from the thermal diffusion formula $g = Cc\lambda / 3$, (where g is the conductivity, C the phonon heat capacity and c the velocity of sound), the phonon mean free path of the beam λ is plotted in Fig. 33. We note that the mean free path is even shorter than the case of GaAs as studied in previous sections. This is because, in addition to the surface scattering, the amorphous nature of the SiN also contribute to further phonon scattering. The result is consistent with thermal conductance measurement of SiN membranes.

The thermal relaxation time, as mentioned before, is much longer than what is anticipated due to the large heat capacity from the tunneling states. The thermal relaxation time increases dramatically when temperature falls below 1 K. This is an indication that the extra heat capacity is *not* effective for energy transport, i.e., the degrees of freedom that contribute to the heat capacity do not contribute to the heat conduction. This is consistent with our explanation that the extra heat capacity comes from the motional tunneling states of the ions.

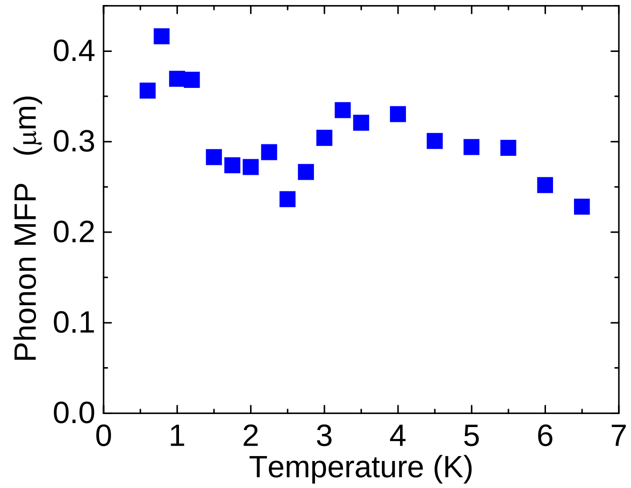

Fig. 33 Phonon mean free path in the SiN calorimeter

3.8 The resolution of the SiN calorimeter

The striking feature of our SiN calorimeter, as compared to existing ones, lies in its high resolution of 0.5 aJ/K. In this section, we will first derive the theoretical resolution and then compare it with experimental measurements.

3.8.1 The calculated resolution of heat capacity measurement

The resolution of the heat capacity measurement is:

$$\Delta C = G\Delta\tau + \tau\Delta G \approx G\Delta\tau \qquad \text{Eq. 30}$$

$$\Delta C = \Delta\tau\ C / \tau$$

this is because the relative error in thermal conductance G is small compared to that of thermal relaxation time τ because the former is a steady state quantity (with long average time) while the later is a dynamic quantity (with relatively shorter average time). Next:

$$\Delta\tau/\tau = \Delta T/3T = V_n/3V_s \qquad \text{Eq. 31}$$

The factor of 3 arises from improvement in accurancy due to fitting. It assumes data are sampled at a period of $\tau/4$ for duration of 4τ, which is typical in our measurement.

Finally, the noise of the measurement is dominated by the hopping noise of the thermometer which is $v_n \approx 10\ \text{nV}/\sqrt{\text{Hz}}$ from 10 to 500 kHz. The signal voltage is $V_s = I\ P\ dR/dT\ /\ G$. Thus, we conclude that:

$$\begin{aligned}\Delta C &= \frac{v_n\sqrt{BW}}{\sqrt{N}v_{Th}}C \\ &= \frac{v_n\sqrt{2CG^{3/2}}}{\sqrt{N}P_H I_{Th}\partial R_{Th}/\partial T}\end{aligned} \qquad \text{Eq. 32}$$

According to the equation, the resolution improves at lower temperature. This comes mainly from the reduction in heat capacity and thermal conductance and improved thermometer sensitivity at low T. However, for temperatures below 1.5 K, the thermometer probe current becomes severely limited by the electron heating. This greatly degrades the signal from the thermometer and reduces the resolution of the thermometer.

As an example, at 2K, the heater current is I_H = 1.5 μA, the thermometer bias current is I_{Th} = 20 nA, the heat capacity is C = 3.75 fJ/K, the thermal conductance is G = 0.1 nW/K and the thermometer sensitivity is dR/dT = -3500 Ω/K. Thus, the thermometer signal is v_{Th} = 34.7 μV. At a BW of 1MHz, this gives a resolution of 0.34 aJ/K.

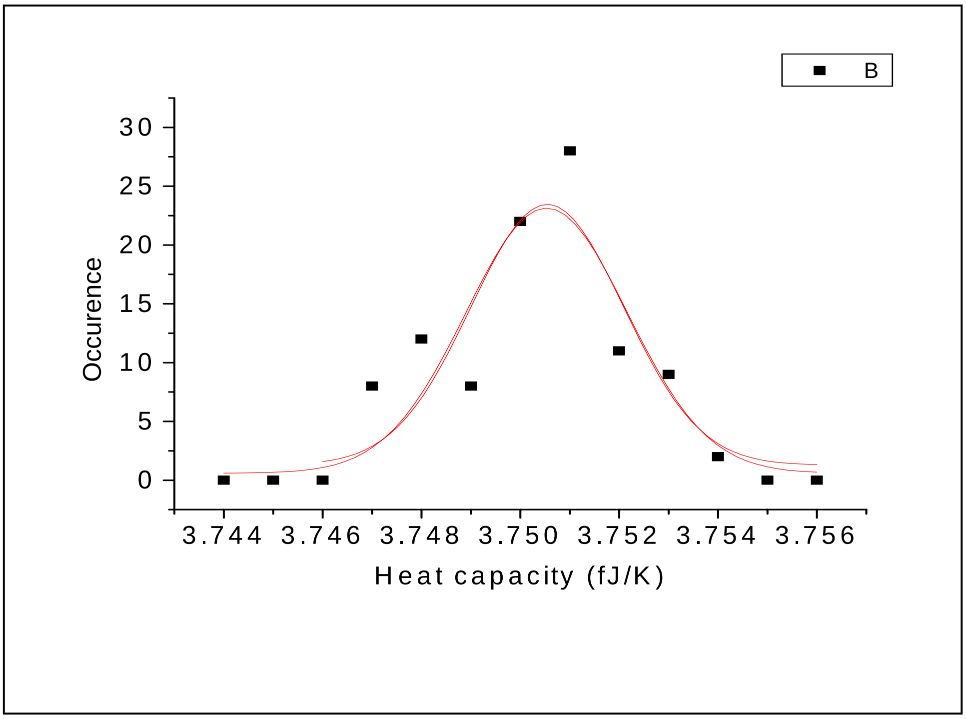

Fig. 34 The histogram of distribution of data measured at 2 K

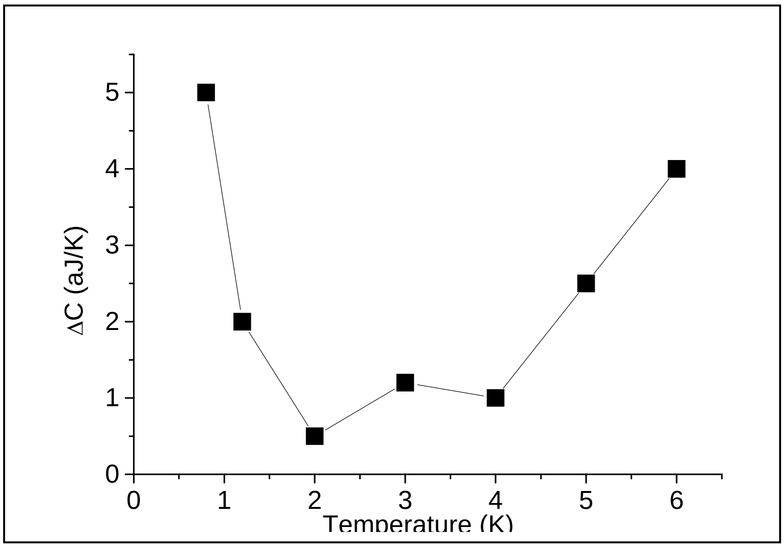

Fig. 35 The resolution of the SiN calorimeter. 100K averages is assumed

3.8.2 The measured resolution of the SiN calorimeter

We could also determine the resolution of the calorimeter from the experimental variance of the data. First, we extract heat capacity result from trace that are moderately averaged for 1000 times (we do not extract data from a single trace measurement because it is too noisy to be fitted). The data is then plotted as a histogram and a Gaussian fit is applied. An example is plotted in Fig. 34 for 100 heat capacity data point obtained at 2 K (Note that since each data is an average of 1000 traces, the histogram actually represent 100,000 measurements). We obtain the error of measurement as $\Delta C = w / \sqrt{N}$, where w is the width of the Gaussian distribution and N is number of data point (= 100 in the example). We thus conclude that the resolution at 2 K is 0.5 aJ/ K. We plot the resolution of the calorimeter versus temperature in Fig. 35. As expected, the resolution is optimum at ~ 2 K.

3.9 Improvement in calorimeter resolution

We briefly discuss possible improvement on the calorimeter. Reduction of the addendum heat capacity is helpful in improving the resolution of the heat capacity measurement. This could be achieved by reducing the volume of the calorimeter either by area reduction during lithography or the choice of a thinner membrane. However, even more effectively in reducing the addendum is to choose a material of lower heat capacity. As discussed above, the major source of heat capacity of SiN comes from the ion motional tunneling states. This could be significantly reduced if a crystalline material, such as silicon, silicon carbide or diamond is used to replace SiN.

It may not be easy to reduce the hopping noise in the thermometry without a significant sacrifice in the thermometer sensitivity. However, we may be able to reduce its effect by reducing the thermal relaxation time constant and move up the measurement frequency, since the hopping noise is much smaller above 2 MHz.

3.10 Application of SiN calorimeter for ^{4}He film heat capacity measurement

We demonstrate in this section the application of the calorimeter to the measurements of the heat capacity of an adsorbed He film. Adsorbed films of He is deposited on the device by means of controlled gas pressure. A buffering chamber of He gas (≈ 0.1 mT) is connected to the cryostat at room temperature. Because of the thermomolecular pressure effect, effective pressure surrounding the device is only 20% of room pressure. While the calorimeter is heated to 6 K, the He gas is introduced into the cryostat to resulting in a coverage of ≈ 2 atoms/nm^2. After the heat capacity measurement at 6 K is finished, the device is cooled to 4 K and the chamber pumped down to 0.1 mT to maintain constant coverage. Then, the buffering chamber is sealed off from the cryostat before further cool down. Below 4 K, the further condensation of He gas increases the coverage only very slightly, by 0.2 atoms/nm^2.

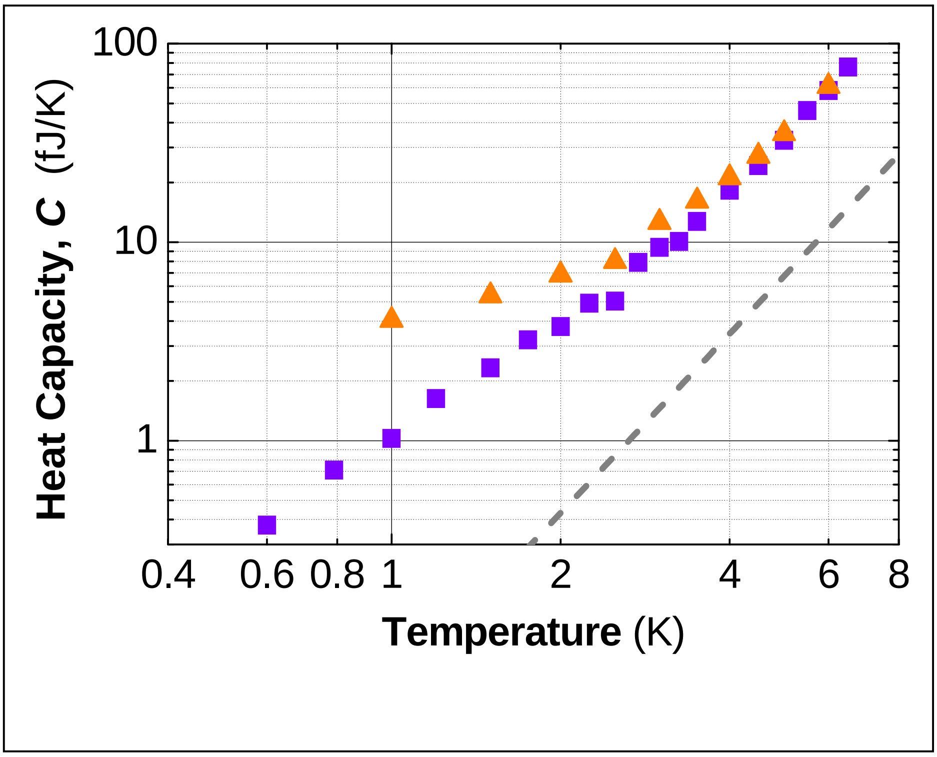

Fig. 36 The measured heat capacity of the ^{4}He film + calorimeter (triangle) and calorimeter alone (square)

The measured heat capacity of the He adsorbed film is shown in Fig. 36. The heat capacity of the film is measured to be ≈ 3 fJ/K. This corresponds to a heat capacity of 1.4 k_B per helium atom. The adsorbed helium gas evidently behaves like a two dimensional ideal gas as similar to the case of He adsorbed on grafoil.[25]

3.11 Conclusion

To conclude, we have developed an ultrasensitive calorimeter with a measured resolution of 0.5 aJ/K at 2 K. We demonstrate its operation by measuring an adsorbed thin film of ^{4}He gas. The device offer potential applications for heat capacity measurement of nanostructures and for sensitive bolometry.

---

[1] Liang WJ, Bockrath M, Bozovic D, Hafner JH, Tinkham M, Park H. NATURE 411 (6838): 665-669 JUN 2001

[2] Cui Y, Wei QQ, Park HK, Lieber CM**.** SCIENCE 293 (5533): 1289-1292 AUG 17 2001

[3] Turberfield AJ, Mitchell JC, Yurke B, Mills AP, Blakey MI, Simmel FC. PHYS REV LETT 90 (11): art. no. 118102 MAR 21 2003

[4] Huang XMH, Zorman CA, Mehregany M, Roukes ML. NATURE 421 (6922): 496-496 JAN 30 2003

[5] Dresselhaus MS, Lin YM, Rabin O, Dresselhaus G**.** MICROSCALE THERM ENG 7 (3): 207-219 JUL-SEP 2003

[6] .S. Tighe, J.M. Worlock, and M.L. Roukes, Appl. Phys. Lett. **70**, 2687 (1997).

[7] K. Schwab, E.A. Henriksen, J.M. Worlock, and M.L. Roukes, Nature (London) **404**, 974 (2000).

[8] W. Fon, K. C. Schwab, J. M. Worlock, and M. L. Roukes, PHYSICAL REVIEW B **66**, 045302 (2002)

[9] W. Fon, K. C. Schwab, J. M. Worlock, and M. L. Roukes, Appl Phys Let, *to be published.*

[10] M.G. Holland, Phys. Rev. **132**, 2461 (1963)

[11] R.O. Carlson, G.A. Slack, and S.J. Silverman, J. Appl. Phys. **36**, 505 (1965).

[12] C.G. Smith, H. Ahmed, and M.N. Wybourne, J. Vac. Sci. Technol. B **5**, 314 (1987).

[13] A. Potts *et al.*, Semicond. Sci. Technol. **7**, B231 (1992).

---

[14] R. Berman, *Thermal Conduction in Solids* Oxford University Press, Oxford, 1976, Chap. 4.

[15] M.G. Holland, Phys. Rev. **134**, A471 (1964).

[16] J.M. Ziman, Philos. Mag. **1**, 191 (1956).

[17] See, for example, Y.J. Han, Phys. Rev. B **54**, 8977 (1996) for a discussion of various forms of the phonon-phonon scattering rate.

[18] J. M. Ziman, *Electrons and Phonons* ~Oxford University Press, Oxford, (1960).

[19] D. W. Denlinger, E. N. Abarra, Kimberly Allen, P. W. Rooney, M. T. Messer, S. K. Watson, and F. Hellman, Rev. Sci. Instrum. **65,** 946 (1994).

[20] C. E. Borroni-Bird and D. A. King, Rev. Sci. Instrum. **62, 2177** (1991).

[21] C. S. Yung, D. R. Schmidt, and A. N. Cleland, Appl. Phys. Lett. **81**, 31 (2002).

[22] X. X. Wang, M. Getaneh, C. J. Martoff and E. Kaczanowicz, J. Appl. Phys. **85**, 8274 (1999).

[23] W. Holmes, J. M. Gildemeister, P. L. Richards and V. Kotsubo, Appl. Phys. Lett. **72**, 2250 (1998).

[24] . C. Zeller and R. O. Pohl, Phys. Rev. B **4**, 2029 (1971).

[25] R. L. Elgin and D. L. Goodstein, Phys. Rev. A **9**, 2657 (1974).